

**Inclusive production of charged pions in p+C collisions at 158 GeV/c  
beam momentum**

C. Alt<sup>7</sup>, B. Baatar<sup>6</sup>, D. Barna<sup>3</sup>, G. Barr<sup>10</sup>, J. Bartke<sup>4</sup>, L. Betev<sup>8</sup>, H. Białkowska<sup>13</sup>, C. Blume<sup>7</sup>,  
B. Boimska<sup>13</sup>, J. Bracini<sup>2</sup>, R. Bramm<sup>7</sup>, P. Bunčić<sup>8</sup>, V. Cerny<sup>2</sup>, P. Christakoglou<sup>1</sup>, O. Chvala<sup>11</sup>,  
P. Dinkelaker<sup>7</sup>, J. Dolejsi<sup>11</sup>, V. Eckardt<sup>9</sup>, H.G. Fischer<sup>8</sup>, D. Flierl<sup>7</sup>, Z. Fodor<sup>3</sup>, P. Foka<sup>5</sup>,  
V. Friese<sup>5</sup>, M. Gaździcki<sup>7</sup>, G. Georgopoulos<sup>1</sup>, C. Höhne<sup>5</sup>, A. Karev<sup>8,9</sup>, S. Kniege<sup>7</sup>,  
T. Kollegger<sup>7</sup>, V.I. Kolesnikov<sup>6</sup>, E. Kornas<sup>4</sup>, M. Kowalski<sup>4</sup>, I. Kraus<sup>5</sup>, M. Kreps<sup>2</sup>, L. Litov<sup>12</sup>,  
M. Makariev<sup>12</sup>, A.I. Malakhov<sup>6</sup>, M. Mateev<sup>12</sup>, G.L. Melkumov<sup>6</sup>, M. Mitrovski<sup>7</sup>, G. Pála<sup>3</sup>,  
A.D. Panagiotou<sup>1</sup>, D. Panayotov<sup>12</sup>, C. Pattison<sup>10</sup>, A. Petridis<sup>1</sup>, R. Renfordt<sup>7</sup>, A. Rybicki<sup>4</sup>,  
A. Sandoval<sup>5</sup>, N. Schmitz<sup>9</sup>, P. Seyboth<sup>9</sup>, F. Siklér<sup>3</sup>, R. Stock<sup>7</sup>, H. Ströbele<sup>7</sup>, J. Sziklai<sup>3</sup>,  
P. Szymanski<sup>8,13</sup>, V. Trubnikov<sup>13</sup>, D. Varga<sup>8</sup>, M. Vassiliou<sup>1</sup>, G.I. Veres<sup>3</sup>, G. Vesztergombi<sup>3</sup>,  
D. Vranić<sup>5</sup>, S. Wenig<sup>8\*</sup>, A. Wetzler<sup>7</sup>, J. Zaraneek<sup>7</sup>

*(The NA49 Collaboration)*

<sup>1</sup>Department of Physics, University of Athens, Athens, Greece.

<sup>2</sup>Comenius University, Bratislava, Slovakia

<sup>3</sup>KFKI Research Institute for Particle and Nuclear Physics, Budapest, Hungary

<sup>4</sup>The H. Niewodniczański Institute of Nuclear Physics, Polish Academy of Sciences, Cracow,  
Poland

<sup>5</sup>Gesellschaft für Schwerionenforschung (GSI), Darmstadt, Germany.

<sup>6</sup>Joint Institute for Nuclear Research, Dubna, Russia

<sup>7</sup>Fachbereich Physik der Universität, Frankfurt, Germany

<sup>8</sup>CERN, Geneva, Switzerland

<sup>9</sup>Max-Planck-Institut für Physik, Munich, Germany

<sup>10</sup>University of Oxford, Oxford, UK

<sup>11</sup>Institute of Particle and Nuclear Physics, Charles University, Prague, Czech Republic

<sup>12</sup>Atomic Physics Department, Sofia University St. Kliment Ohridski, Sofia, Bulgaria

<sup>13</sup>Institute for Nuclear Studies, Warsaw, Poland

**Abstract**

The production of charged pions in minimum bias p+C interactions is studied using a sample of 377 000 inelastic events obtained with the NA49 detector at the CERN SPS at 158 GeV/c beam momentum. The data cover a phase space area ranging from 0 to 1.8 GeV/c in transverse momentum and from -0.1 to 0.5 in Feynman x. Inclusive invariant cross sections are given on a grid of 270 bins per charge thus offering for the first time a dense coverage of the projectile hemisphere and of the cross-over region into the target fragmentation zone.

\*) Corresponding author: Siegfried.Wenig@cern.ch



## 1 Introduction

The study of p+A interactions represents an important part of the NA49 experimental programme which is aimed at a comprehensive study of soft hadronic interactions covering both elementary and nuclear collisions. In the framework of this programme a first paper on inclusive pion production in p+p collisions has been published recently [1]. The present study extends these measurements to p+C interactions. The use of the isoscalar, light  $^{12}\text{C}$  nucleus has several motivations. Firstly, it allows inspection of the evolution from elementary to nuclear collisions for a small number of intranuclear projectile interactions as compared to the high-statistics data sets on the heavy  $^{208}\text{Pb}$  nucleus from the NA49 experiment [2]. Secondly, it satisfies, at least partially, the need of high precision p+A reference data from light nuclei for the control of systematic effects in neutrino physics. This applies both to long baseline neutrino oscillation experiments using light neutrino production targets (e.g. [3] which uses a beam energy of 120 GeV) and to atmospheric neutrino studies [4]. In the latter case the  $^{12}\text{C}$  nucleus is sufficiently close to  $^{14}\text{N}$  and  $^{16}\text{O}$  to allow a sensible test of the different hadronic production models developed for the interpretation of these data [5].

The NA49 p+C data sample consists of 377 000 inelastic events corresponding to only 8% of the event number available in p+p collisions [1]. The reasons for this relatively limited statistics lie entirely in the heavy restrictions which the SPS fixed-target programme as a whole has suffered over the past years. These restrictions concern both the beam availability and the choice of topics in hadronic physics acceptable to the relevant committee [6]. In view of the almost total absence of existing data in the SPS energy range [7, 8] the NA49 results nevertheless constitute a unique extension of the present knowledge in the sector of p+A interactions with light nuclei.

The present study is closely related to the preceding publication on pion production in p+p interactions [1] which is recommended as a reference for the description of most experimental details. Only those items which are specific for p+C collisions will be touched upon here. The layout of the paper is arranged as follows. After a short comment concerning the situation of previous measured data in Sect. 2, Sect. 3 describes the parts of the NA49 experiment which differ from the p+p data taking. Sect. 4 deals with the determination of the inclusive cross sections and the applied corrections. The final data are presented and compared to other experiments in Sects. 5 and 6. The  $p_T$  integrated distributions are evaluated for minimum bias condition in Sect. 7 and Sect. 8 describes the dependence on the measured number of grey protons.

## 2 The Experimental Situation

The asymmetric nature of p+A interactions necessitates in principle a complete coverage of the target and projectile hemispheres in order to experimentally constrain the underlying production mechanism. The phase space coverage of existing data in p+C is even more restricted than for p+p collisions [1]. In fact there are only two sets of data in the SPS energy range offering double differential inclusive cross sections for identified pions,

$$\frac{d^2\sigma}{dx_F dp_T^2}, \quad (1)$$

where the longitudinal scaling variable  $x_F = 2p_L/\sqrt{s}$  is defined in the nucleon-nucleon cms.

The first data set at 400 GeV/c beam momentum covers the far backward region at a number of fixed laboratory angles [8], yielding important information about the region of intranuclear cascading. The second one presents a small number of data points in the far forward

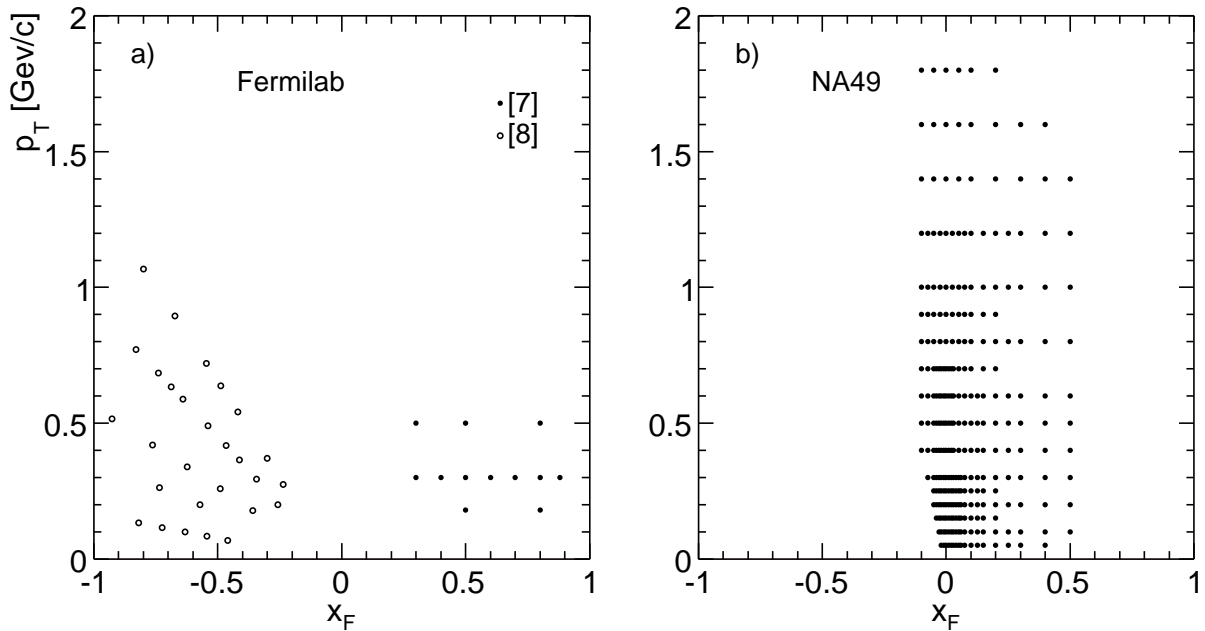


Figure 1: Phase space coverage of existing data in a) Fermilab and b) NA49

region [7]. The situation is depicted in Fig. 1a which shows that there are no data in the complete central region  $-0.2 < x_F < 0.3$ .

The new NA49 results fill this gap to a large extent, as shown in Fig. 1b. They are limited to  $p_T < 1.8$  GeV/c and to  $x_F < 0.5$  essentially by the modest event statistics, see Sect. 1. In the backward hemisphere, a  $p_T$  dependent cut at  $x_F > -0.1$  is imposed both by the NA49 acceptance and by the particle identification via ionization energy loss. Nevertheless an inspection of the important cross-over region between projectile and target hemispheres is possible.

### 3 Parts of the NA49 experiment specific to p+C interactions

Most parts of the NA49 experimental setup and of the data processing procedure are identical for p+p and p+A data taking. This concerns the beam definition, the interaction trigger scheme, tracking, event reconstruction and selection, and particle identification [1]. The experimental items which are specific to the p+C data taking are described below.

#### 3.1 Target and grey proton detection

A graphite target of 0.7 cm length and 0.6 cm diameter with a density of  $1.83 \text{ g/cm}^3$  has been used. This corresponds to an interaction length of 1.5%. The target is housed inside a grey proton detector [9] which has been developed for the control of impact parameter (centrality) in p+A collisions and is presented schematically in Fig. 2.

This detector is a cylindrical proportional counter of 12 cm diameter which surrounds the target and has a window in the forward hemisphere corresponding to the acceptance of the spectrometer inside polar angles of  $< 45^\circ$ . Its surface is subdivided into 256 pads which provides ample granularity for the counting of the typically less than 8 grey protons measured per event in light ion applications. A thin (200  $\mu\text{m}$ ) copper sheet on the inner surface absorbs nuclear fragments by range, and an electronics threshold placed at 1.5 times the minimum ionization deposit cuts high momentum particles as the grey protons are placed high on the  $1/\beta^2$  branch of the Bethe-Bloch energy-loss distribution. Grey protons in the momentum range 0.15

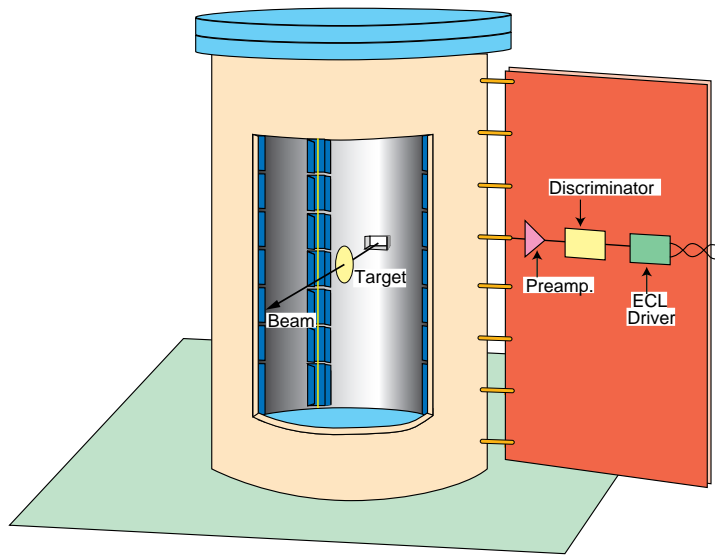


Figure 2: Centrality detector

to 1.2 GeV/c reconstructed and identified inside the spectrometer acceptance are added to the number measured in the centrality detector.

The resulting number distribution is shown in Fig. 3, together with the prediction by Hegab and Hüfner [10] for the total grey proton yield and the measurement by Braune et al. [11] at 50 and 100 GeV/c beam momentum at the SPS using a detector of 60% geometrical acceptance. Compared to this the NA49 data correspond to a 45% effective acceptance which is in part due to the steep angular distribution of slow protons in p+C collisions [11] and to the

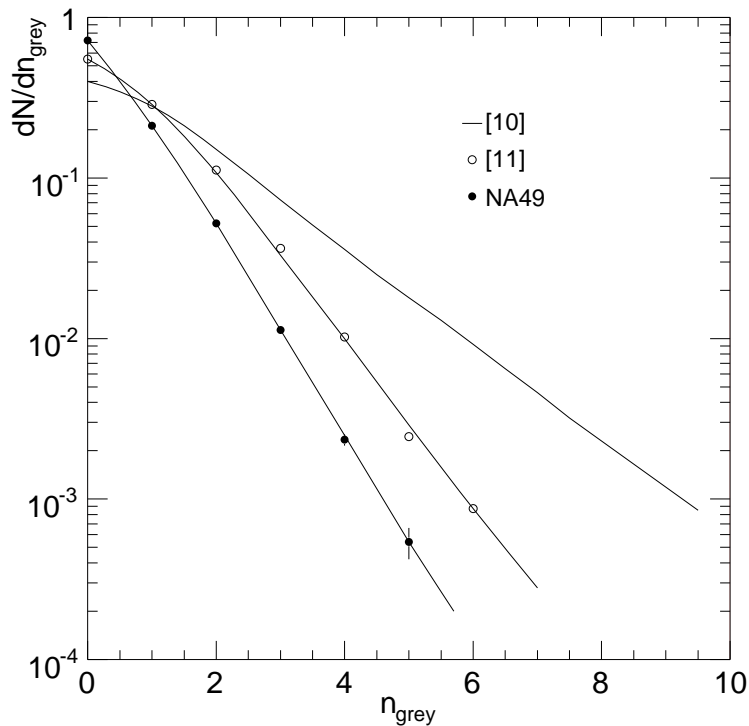


Figure 3: Number of grey protons  $n_{\text{grey}}$  distribution. The lines through the data points are drawn to guide the eye

large opening of  $\pm 45^\circ$  imposed by the spectrometer acceptance. Only about 30% of protons in this angular range with momenta below 1 GeV/c are in fact reconstructed and identified by the NA49 tracking system.

Due to the short available data taking period and to the sharp drop of the event yield as a function of the number of grey protons (less than 30% of all events have a measured grey proton), the on-line triggering capability on grey protons available in the NA49 trigger system could not be used. All data have therefore been obtained in “minimum bias” condition without imposing centrality selection. It is nevertheless possible to use the grey proton information in a sample of  $p_T$  integrated inclusive cross sections in order to study the evolution with centrality as described in Sect. 8.

As the range of grey protons at their most probable momentum of 0.3 GeV/c is only 1 cm in Carbon, the target diameter of 6 mm has been kept at a minimum with respect to the transverse beam profile [1] in order to reduce the absorption of grey protons by energy loss in the target material. The small fraction of beam particles in the tail of the transverse profile beyond the target radius ( $\approx 3\%$ ) has been corrected for in the determination of the trigger cross section.

### 3.2 Trigger cross section

The trigger scheme was the same as in p+p interactions, using an interaction trigger defined by a small scintillation counter 380 cm downstream of the target in anti-coincidence with the beam. Due to the reduction of forward protons in p+A interactions by baryon number transfer towards central rapidities and due to the corresponding yield decrease of produced particles at large  $x_F$ , the systematic effects connected to this trigger method are smaller than in p+p collisions and amount to a reduction of the trigger cross section of  $9\% \pm 2\%$  with respect to the total inelastic cross section. A break down of these losses determined by using measured inclusive distributions of protons, pions and kaons [17] in a Monte Carlo calculation, is given in Table 1.

$\sigma_{\text{trig}}$	210.1 mb
loss from p	17.1 mb
loss from $\pi$ and K	2.4 mb
contribution from $\sigma_{\text{el}}$	-3.3 mb
predicted $\sigma_{\text{inel}}$	226.3 mb
literature value	225.8 mb

Table 1: Contributions derived from the detailed Monte Carlo calculation to the determination of the measured inelastic cross section  $\sigma_{\text{inel}}$

The resulting measured value of the inelastic p+C cross section is 226.3 mb with an estimated systematic error of 2.5% (see Table 3). It compares well with a compilation of preceding measurements [13] giving 225.8 mb as shown in Fig. 4.

The relatively large systematic deviations visible in the reference values, which have all been obtained in transmission experiments using yield extrapolation to zero momentum transfer, is noteworthy. It is partially attributable to the definition of the elastic component and to the corresponding uncertainty in the slopes of the  $t$ -distributions used. Compared to the precision available in the elementary hadron-nucleon inelastic cross sections, the absolute normalization of inclusive yields therefore suffers from larger systematic uncertainties.

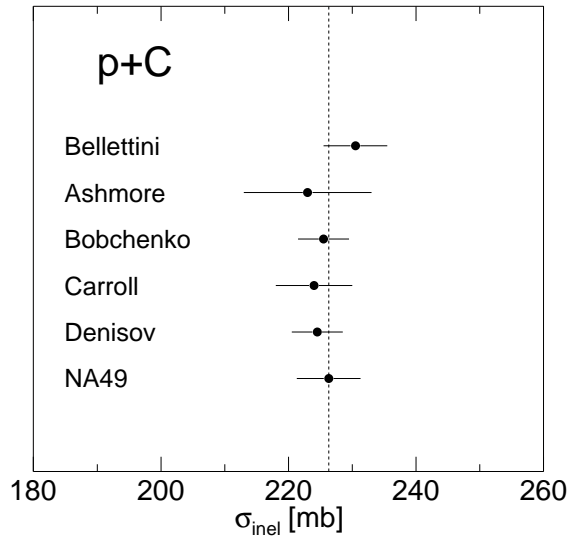


Figure 4: Inelastic cross section compared to previous measurements [13]

### 3.3 Event sample and cuts

In addition to the cuts imposed on the transverse beam definition as obtained from the Beam Position Detectors [9] an additional cut on the transverse beam radius at less than 3 mm is imposed due to the target dimension (Sect. 3.1). The longitudinal vertex position is constrained to a fiducial region, as exemplified for two values of charged multiplicity in Fig. 5, where the distribution of detector material in the vicinity of the target is clearly visible.

The combined cuts result in the event sample given in Table 2 where in particular the

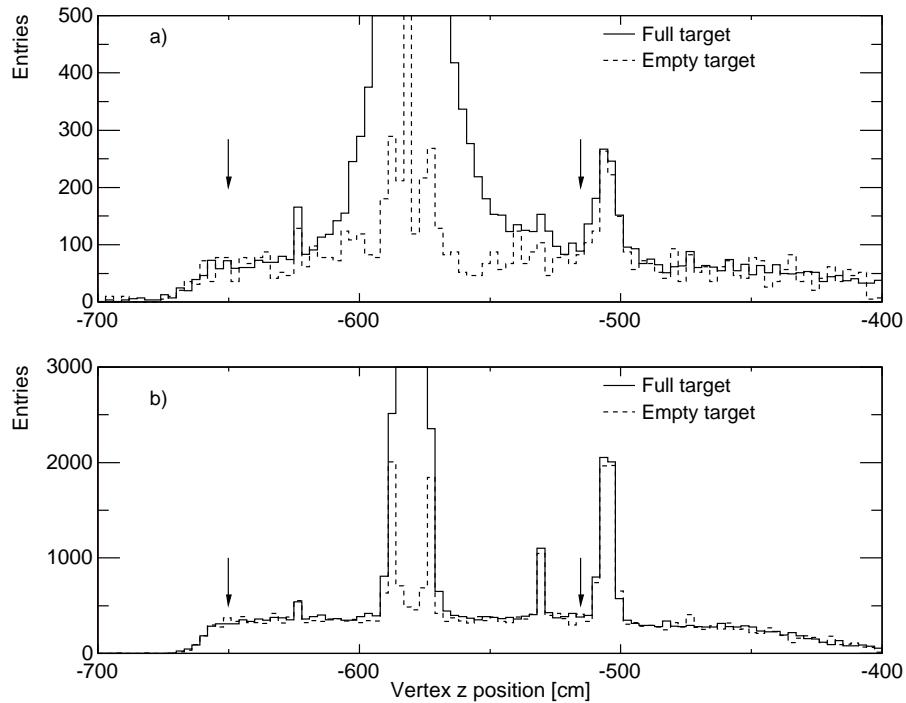


Figure 5: Normalized vertex distributions from full and empty target events with selected track multiplicity a) one and b) five and more. The arrows indicate the fiducial region

reduction of the empty target fraction from 30% in the total sample to 16% after cuts is noteworthy. Due to the small correction imposed by the empty target contribution (see Sect. 4.1), the fraction of running time spent on empty target could be kept at about 5% only.

Events taken		Events after selection	
Full target	Empty target	Full target	Empty target
535.7 k	31.2 k	377.6 k	11.8 k

Table 2: Data sample

### 3.4 Acceptance coverage, binning and statistical errors

Due to the forward-backward asymmetry of p+A interactions a substantial effort was spent in exploiting the available acceptance in the region of negative  $x_F$ . Here limitations are imposed both by the detector acceptance itself and by the particle identification problems in the region near minimum ionization. The resulting phase space coverage with 270 bins per charge is presented in Fig. 6 where also the statistical errors per bin are indicated.

The reduced statistics compared to the much larger event sample in p+p collisions [1] results in larger bins generally and a limitation to the regions  $p_T \leq 1.8$  GeV/c and  $x_F \leq 0.5$ . It nevertheless provides an unprecedented overall coverage which allows a detailed study of the important cross-over region between target and projectile fragmentation for the first time.

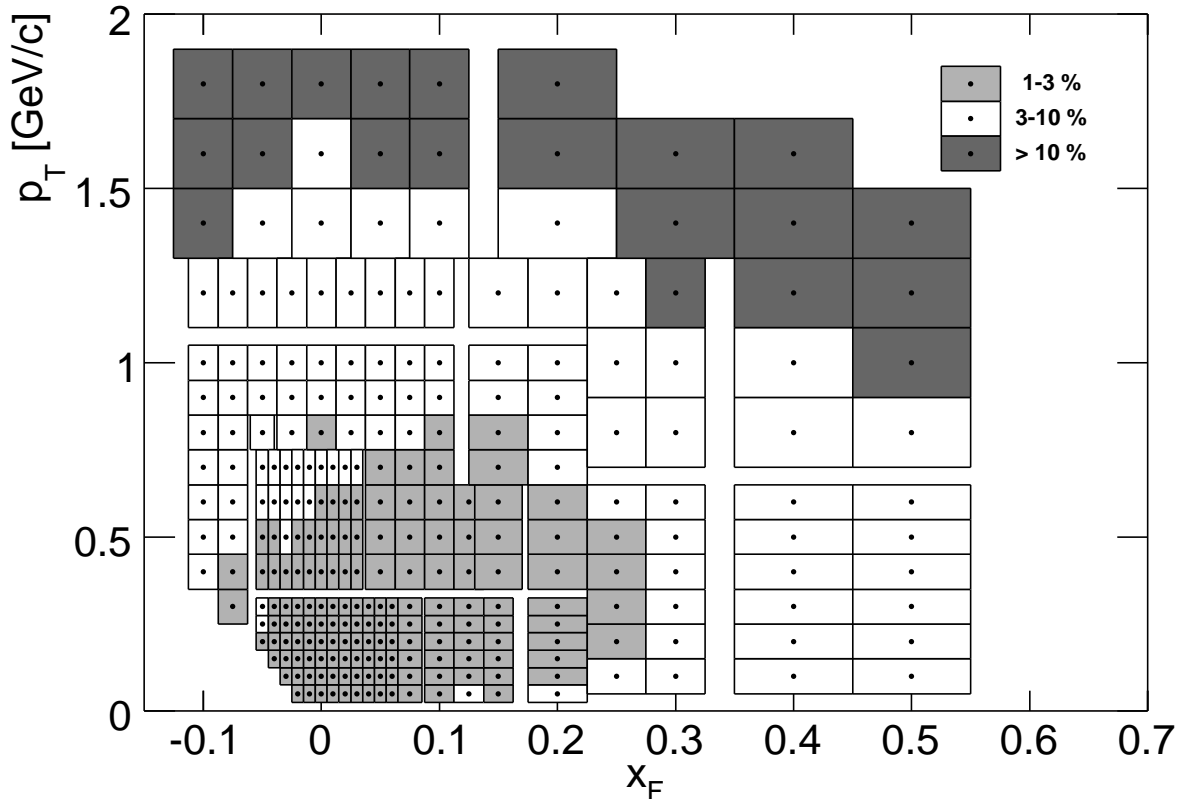


Figure 6: Binning scheme in  $x_F$  and  $p_T$  together with information of the statistical error



### 3.5 Particle identification

The procedures for the extraction of pion yields from the energy loss distributions measured in each bin are identical to the ones used in p+p collisions [1] for most of the forward hemisphere. The extended coverage of the backward hemisphere together with the forward-backward asymmetry of p+C interactions necessitates an extension of the methods developed in [1] for the treatment of the lab momentum region below 3 GeV/c where the energy loss functions of pions, kaons and protons approach each other. The kinematic situation in this region is indicated in Fig. 7.

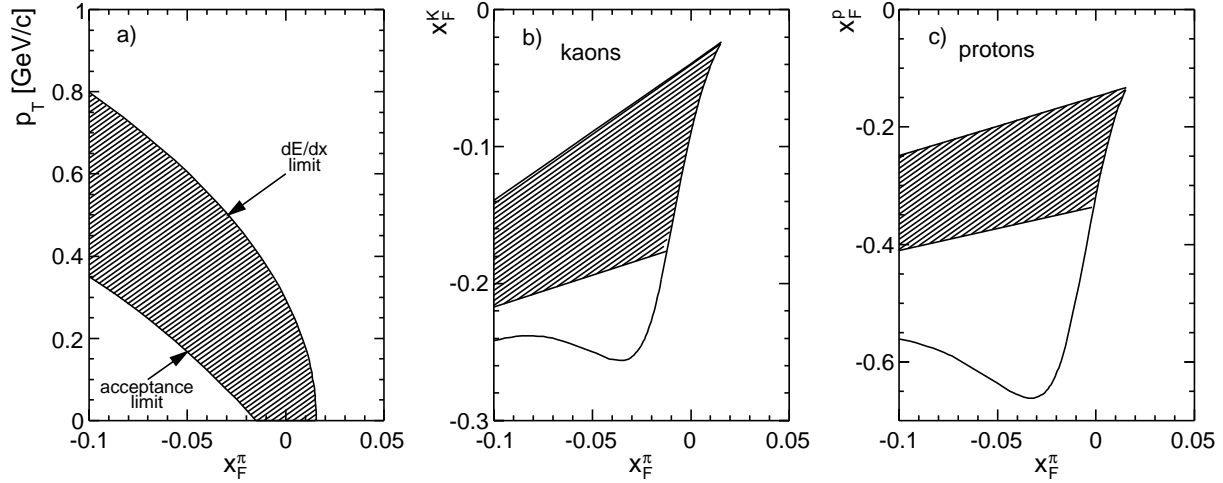


Figure 7:  $dE/dx$  cross-over region: a) in  $(x_F, p_T)$  plane of the pions, b) in  $(x_F^\pi, x_F^K)$  plane, and c) in  $(x_F^\pi, x_F^p)$  plane. The unhatched areas correspond to the regions where pions can be identified due to the  $1/\beta^2$  increase of energy loss of the kaons and protons, respectively

Using the pion mass in the transformation from  $x_F$  to lab momentum the critical zone is defined by the hatched area in Fig. 7a where the upper limit corresponds to  $p_{\text{lab}} = 3$  GeV/c and the lower limit traces the  $p_T$  cut-off used in the data extraction (Fig. 6). This area is mapped into the  $x_F$  regions for kaons (Fig. 7b) and protons (Fig. 7c) as a function of  $x_F^{\text{pion}}$  when using the proper masses in the corresponding Lorentz transformations.

For protons the lower part of the critical zone is again available for  $dE/dx$  extraction due to the rapid increase of their energy loss in the  $1/\beta^2$  region of the Bethe-Bloch function. The

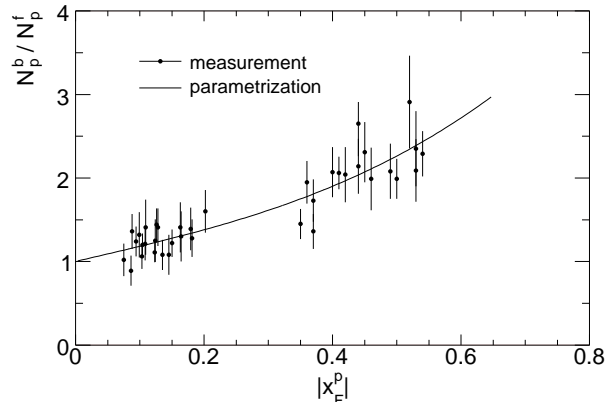


Figure 8: Backward/forward yield ratio for protons

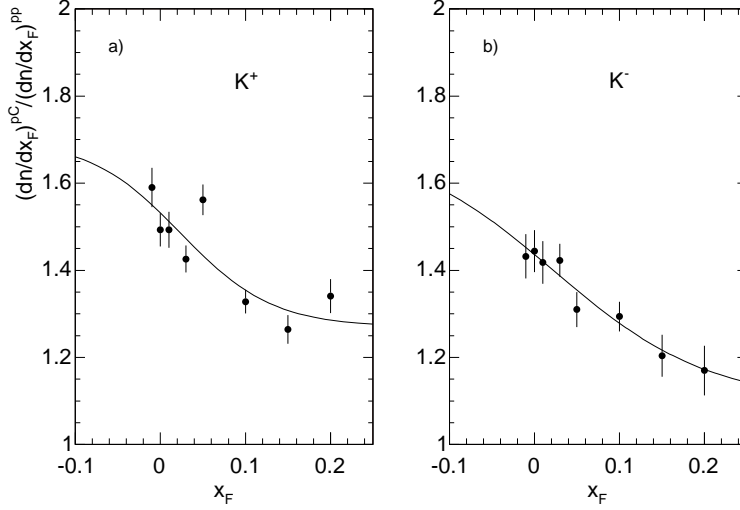


Figure 9:  $(dn/dx_F)^{pC}/(dn/dx_F)^{pp}$  ratio as a function of  $x_F$  of the kaons for a)  $K^+$  and b)  $K^-$

remaining band at  $-0.4 < x_F^{\text{proton}} < -0.2$  is treated by reflecting the  $x_F$  bins into the forward hemisphere and by using an interpolation of the measured backward/forward yield ratios shown in Fig. 8.

The  $\bar{p}/\pi^-$  and  $K/\pi$  ratios are smaller than 10% for all bins in the critical area. Here again the method of bin reflection was used by imposing an extrapolation of the measured yield ratio with respect to p+p interactions into the backward hemisphere as shown in Fig. 9 for kaons. In this case the ratio in the far backward region corresponds to the mean number of projectile collisions predicted from the inelastic p+C and p+p cross sections [12]. For kaons the different loss rates from weak decays in the forward and backward hemispheres were taken into account in the yield determination.

#### 4 Evaluation of invariant cross sections and corrections

The invariant inclusive cross section

$$f(x_F, p_T) = E(x_F, p_T) \cdot \frac{d^3\sigma}{dp^3}(x_F, p_T) \quad (2)$$

is experimentally defined by the measured quantity [1]

$$f_{\text{meas}}(x_F, p_T, \Delta p^3) = E(x_F, p_T, \Delta p^3) \cdot \frac{\sigma_{\text{trig}}}{N_{\text{ev}}} \cdot \frac{\Delta n(x_F, p_T, \Delta p^3)}{\Delta p^3}, \quad (3)$$

where  $\Delta p^3$  is the finite phase space element defined by the bin width.

As in [1] several steps of normalization and correction have to be applied in order to make  $f_{\text{meas}}(x_F, p_T, \Delta p^3)$  approach  $f(x_F, p_T)$ . The determination of the trigger cross section and its deviation from the total inelastic cross section has been discussed above. The corrections for pion weak decay and absorption in the detector material are identical to p+p and will not be discussed here. The remaining corrections which are numerically different in p+C interactions are:

- treatment of empty target contribution
- re-interaction in the target volume
- effect of the interaction trigger

- feed-down from weak decays of strange particles
- effect of finite bin width.

These corrections will be described and quantified below.

#### 4.1 Empty target contribution

In the determination of the normalized quantity

$$\left(\frac{\Delta n}{N_{\text{ev}}}\right)^{\text{FT-ET}} = \frac{1}{1 - \epsilon} \left( \left(\frac{\Delta n}{N_{\text{ev}}}\right)^{\text{FT}} - \epsilon \left(\frac{\Delta n}{N_{\text{ev}}}\right)^{\text{ET}} \right), \quad (4)$$

the ratio  $\epsilon$  of empty over full trigger rates has been reduced from 0.3 to 0.16 by the cuts described in Sect. 3.3 above. In addition, the bulk of the remaining empty target yield is produced in Mylar foils and air (Fig. 5). These materials are sufficiently close to Carbon to make the normalized bin contents  $(\Delta n/N_{\text{ev}})^{\text{FT}}$  and  $(\Delta n/N_{\text{ev}})^{\text{ET}}$  approximately equal. The deviation of the complete normalized yield from the full target yield alone is therefore expected to be small and to be essentially defined by the different fraction of empty events in full and empty target conditions. This is demonstrated in Fig. 10 where the ratio between the bin contents for full-empty target and full target alone is shown as a function of  $x_F$ .

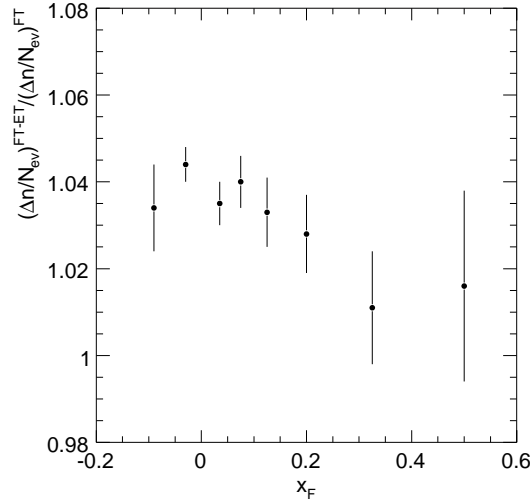


Figure 10: Correction factor applied to account for empty target contribution as a function of  $x_F$  for the average of  $\pi^+$  and  $\pi^-$

Within the limits of the experimental accuracy no differences between  $\pi^+$  and  $\pi^-$  and no dependencies on  $p_T$  have been observed.

#### 4.2 Target re-interaction

The Carbon target has an interaction length of 1.5% which corresponds to only 55% of the length of the hydrogen target used in p+p interactions. The expected re-interaction correction is therefore below the 2% level even in the extreme backwards bins and has been scaled down accordingly from the values obtained in [1].

### 4.3 Trigger bias correction

Several effects contribute to a modification of the correction for the trigger bias which is introduced by the interaction trigger in p+C as compared to p+p collisions. They all lead to a reduction of the correction to the p+C data.

- Due to baryon number transfer towards central rapidity (“stopping”) there are less forward protons hence a smaller probability to veto events by the trigger counter.
- Due to the correlated steepening of the  $x_F$  distributions of produced particles (see Sect. 5) there is again a reduction of the veto probability. These two effects combine to explain the higher inelastic trigger efficiency of 93% in p+C as compared to 89% in p+p collisions.
- Unlike in p+p events, there is a long-range correlation between target fragmentation and forward particle density. Large  $x_F$  protons are correlated with single projectile collisions yielding small backward multiplicities, whereas multiple projectile collisions result in high target multiplicity and low forward yields. This correlation reduces the effect of the interaction trigger in the backward hemisphere.

The trigger bias correction has been obtained using the method developed in [1] by artificially increasing the diameter of the trigger counter in the analysis and extrapolating to surface zero. The resulting corrections are shown in Fig. 11 as a function of  $x_F$  for two values of  $p_T$ . The correction is smaller than in the p+p case [1] and thus confirms the reduction quoted above.

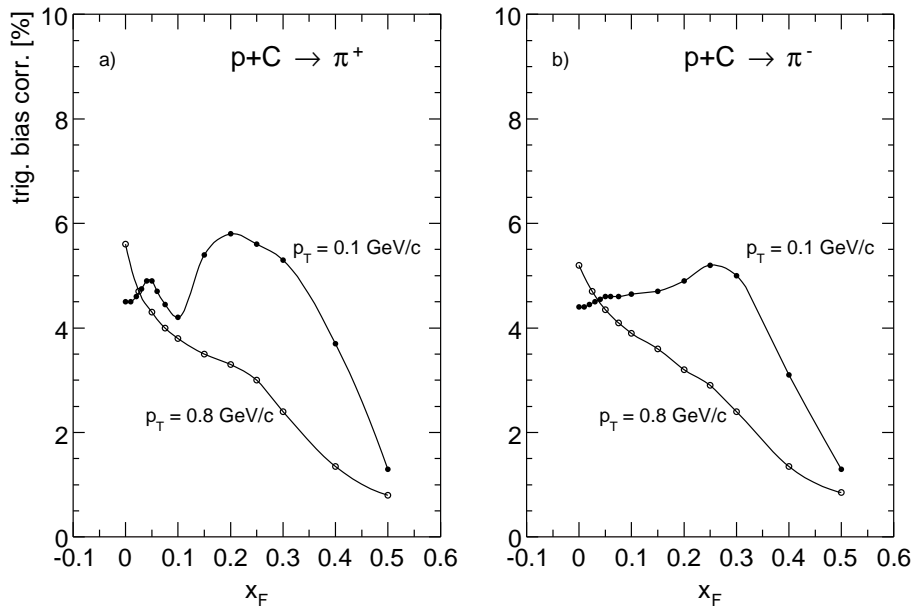


Figure 11: Trigger bias correction as a function of  $x_F$  at various  $p_T$  for a)  $\pi^+$  and b)  $\pi^-$

### 4.4 Feed-down correction

A principle problem in the determination of the feed-down correction induced by the weak decays of strange particles lies in the absence of data on  $K_S^0$  and strange baryon production in light ion collisions. The corresponding yields have therefore been determined from the NA49 data directly using the following yield ratios with respect to p+p interactions:

- The  $K_S^0$  yield is extracted from  $(K^+ + K^-)/2$ . The measured ratio is extrapolated into the backward hemisphere using a two-component superposition picture [2] as shown in

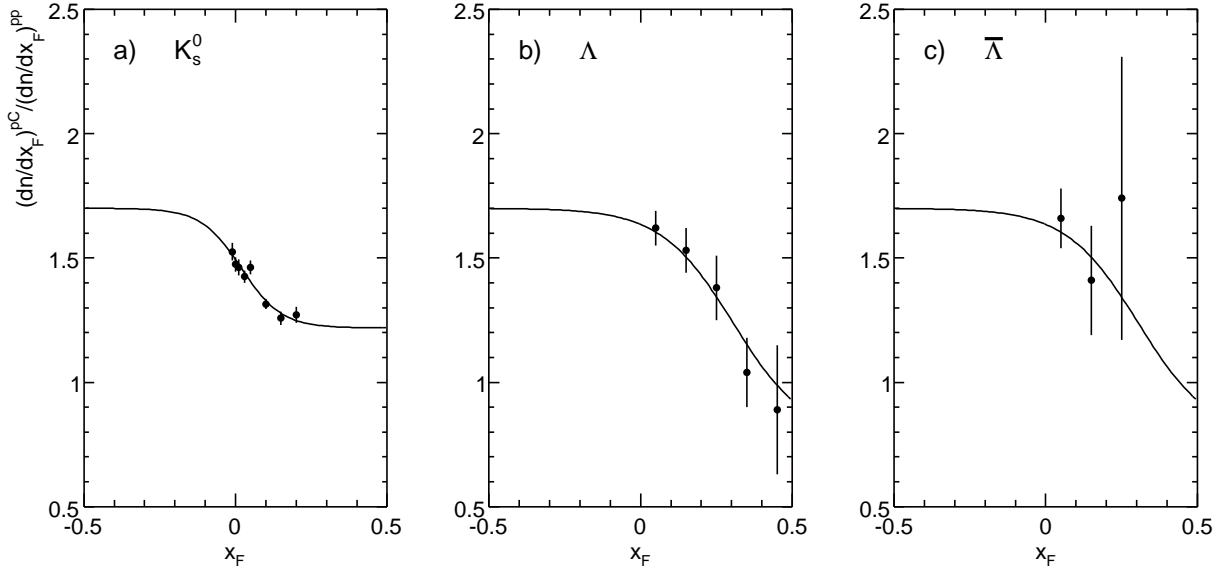


Figure 12: Yield ratios for a)  $K_s^0$ , b)  $\Lambda$  and c)  $\bar{\Lambda}$

Fig. 12a. As the kaon yields do not suffer from isospin effects [2] this extrapolation is straight-forward concerning the target contribution.

- The evolution of  $\Lambda$  and  $\bar{\Lambda}$  yields relative to p+p is obtained from  $p+\pi^-$  and  $\bar{p}+\pi^+$  mass distributions exploiting the event mixing technique described in [15] and using vertex tracks both for the baryon and for the meson involved. The resulting yield ratios are shown in Figs. 12b and c. For the extrapolation into the backward hemisphere the two-component superposition picture is again used. No isospin effects are present in this extrapolation.

The yield ratios for  $\Sigma^\pm$  are derived from the  $\Lambda$  parametrization using the  $\Sigma/\Lambda$  ratios from p+p in the projectile hemisphere. In the target fragmentation region the expected isospin effects are taken into account.

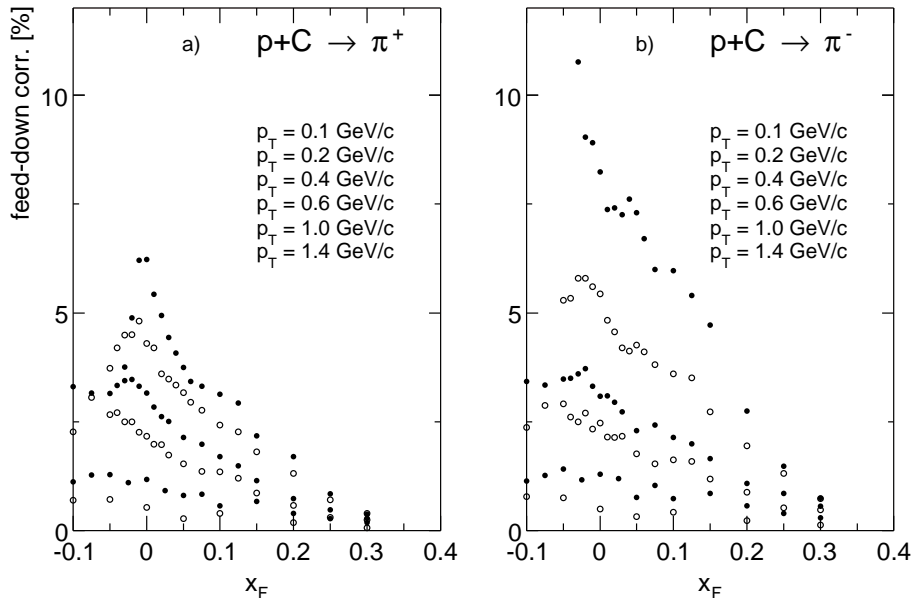


Figure 13: Feed-down correction to pion from weak decays for a)  $\pi^+$  and b)  $\pi^-$

The resulting overall feed-down corrections are shown in Fig. 13 as a function of  $x_F$  for several values of  $p_T$ .

#### 4.5 Binning correction

The correction for finite bin width follows the scheme developed in [1] determining the deviation of the real cross section at the bin center from the measured one (averaged over the bin) using the local second derivative of the particle density distribution. The derivative is calculated using the experimental data and therefore does not depend on specific parametrizations. Typical values of the resulting correction are shown in Fig. 14 for low  $p_T$  as a function of  $x_F$  and for  $x_F = 0$  as a function of  $p_T$ , both for constant bin widths of  $\Delta x_F = 0.02$  and  $\Delta p_T = 0.1$  GeV/c, and for the bin widths actually used in the data extraction.

Due to the increased average bin width in p+C the values are somewhat larger than in p+p, but typically stay below the  $\pm 2\%$  limit, except for  $x_F \geq 0.4$  and  $p_T \geq 1.2$  GeV/c.

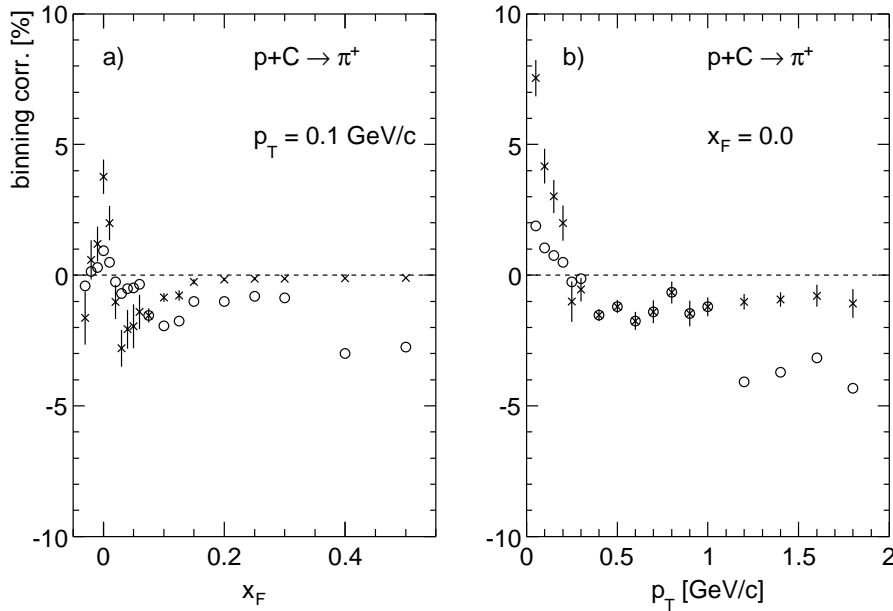


Figure 14: Correction due to the binning in a)  $x_F$  and b)  $p_T$ . The crosses represent the correction at fixed bin widths of  $\Delta x_F = 0.02$  and  $\Delta p_T = 0.1$  GeV/c, respectively and the open circles describe the correction for the bins actually used

#### 4.6 Systematic errors

An estimation of the systematic errors induced by the overall normalization and by the applied corrections is given in Table 3.

An upper limit of 7.5% from linear addition of the error sources and an rms error of 3.8% from quadratic summation are obtained. Further information on the bin-by-bin variation of the different error contributions is contained in Fig. 15 which demonstrates that the single errors fluctuate around well-defined mean values with limited skewness and tails.

### 5 Results

The set of double differential invariant cross sections obtained from the data analysis and correction procedures described above forms, by its dense coverage of the available phase space

Normalization	2.5%
Tracking efficiency	0.5%
Trigger bias	1%
Feed-down	1-2.5%
Detector absorption Pion decay $\pi \rightarrow \mu + \nu_\mu$ Re-interaction in the target	0.5%
Binning	0.5%
Total(upper limit)	7.5%
Total(quadratic sum)	3.8%

Table 3: Summary of systematic errors

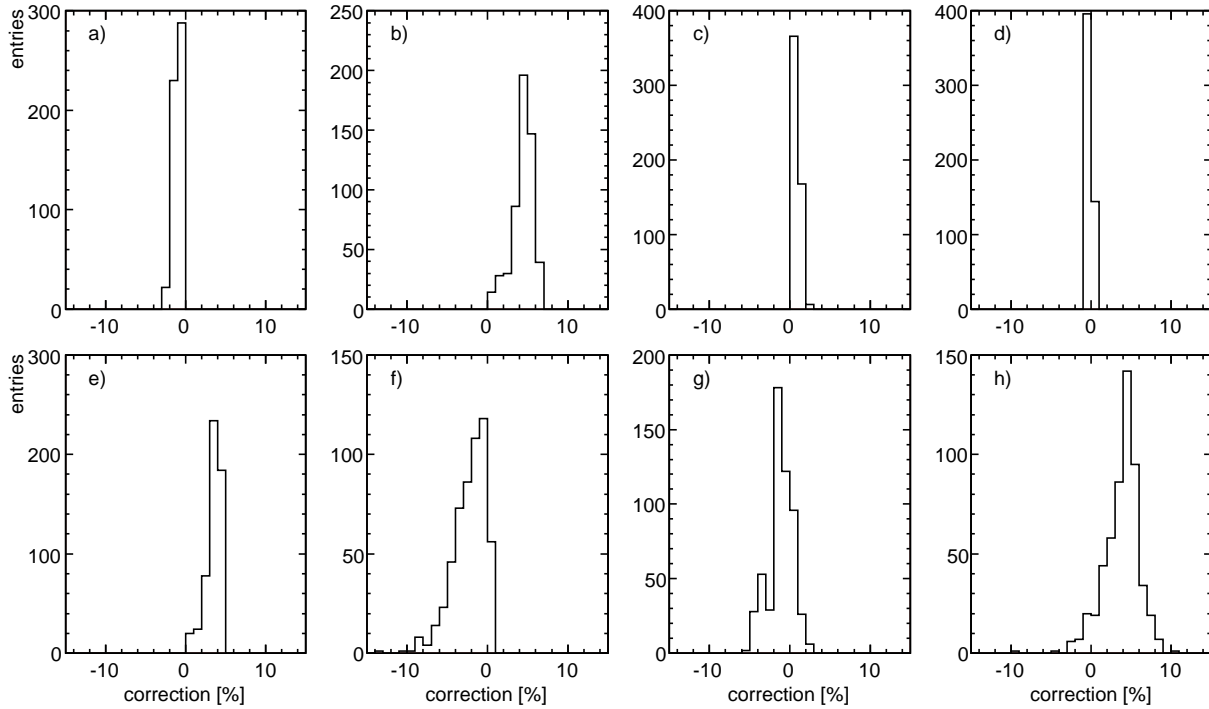


Figure 15: Distribution of correction for a) target re-interaction, b) trigger bias, c) absorption in detector material, d) pion decay, e) empty target contribution, f) feed-down, g) binning, and h) resulting total correction

in 270 bins per charge, an internally consistent ensemble that reveals, as in the case of p+p interactions, complex structures which pervade both transverse and longitudinal momentum dependencies. These structures defy simple parametrization with straight-forward arithmetic expressions. To make full use of the consistency of the data set and to allow for optimum precision in the determination of integrated cross sections, a numerical interpolation scheme has therefore been used that relies on local continuity in both kinematic variables and allows for limited extrapolation into the inaccessible regions of phase space. This chapter summarizes the numerical information in data tables, gives a set of distributions as a function of  $p_T$ ,  $x_F$  and rapidity  $y$ , and shows the comparison to existing data.

## 5.1 Data tables, distributions and interpolation scheme

Tables 4 and 5 present the invariant inclusive cross sections for  $\pi^+$  and  $\pi^-$  respectively. They correspond to the binning scheme discussed in Sect. 3.4 above and reflect the attempt to cover the kinematic plane as completely as possible given the limited statistical accuracy of the data sample.

The distributions of the data in  $p_T$  and  $x_F$  are shown in Figs. 17 and 18 respectively. Here the full lines represent the data interpolation mentioned above.

In order to demonstrate the statistical consistency of the interpolation scheme, the distribution of the differences between data and interpolation, normalized with the statistical error in each data point, is shown in Fig. 16. The shape and width of the distribution comply with the expected Gaussian behaviour.

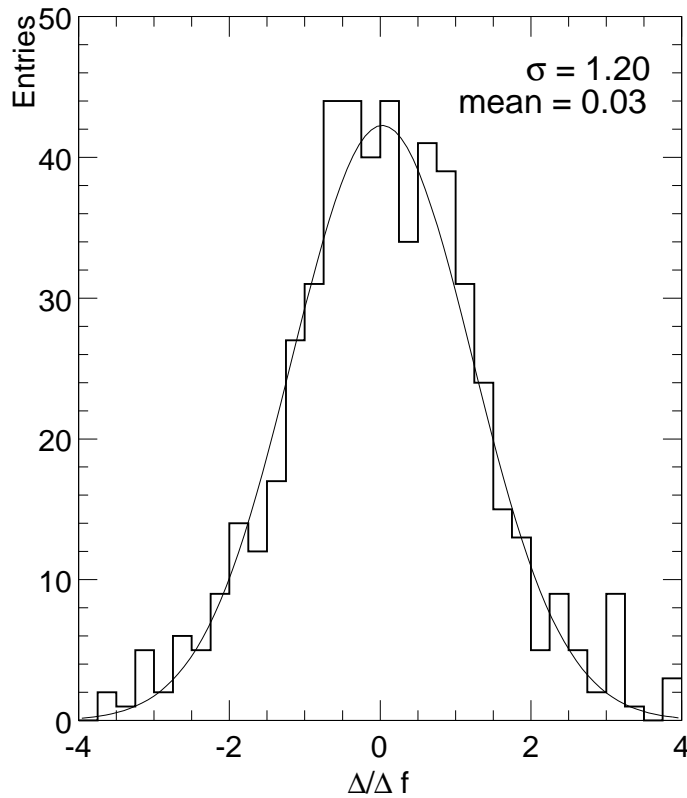


Figure 16: Histogram of the differences  $\Delta$  between the measured invariant cross sections and the corresponding interpolated values ( $\pi^+$  and  $\pi^-$  combined) divided by the experimental uncertainty  $\Delta f$  of the data points

## 5.2 $\pi^+/\pi^-$ ratios

The dependence of the  $\pi^+/\pi^-$  ratio on  $p_T$  and  $x_F$  carries important information concerning the details of charge conservation in the hadronization process. As presented in Figs. 19 and 20, important substructures in both variables become visible which are directly comparable to the situation in p+p interactions [1].



$f(x_F, p_T), \Delta f$									
$p_T \backslash x_F$	-0.1	-0.075	-0.05	-0.04	-0.03	-0.025	-0.02	-0.01	0.0
0.05							589.8 2.41	616.9 2.50	652.3 1.59
0.1					584.0 2.62		611.0 1.77	587.3 1.59	581.7 1.68
0.15				445.2 2.80	488.4 1.89		509.8 1.81	502.0 1.66	508.2 1.55
0.2			353.4 2.99	365.7 2.70	385.2 1.93		403.2 1.85	382.1 1.77	411.9 1.65
0.25			268.6 3.20	284.5 2.55	308.2 2.28		287.1 2.14	300.3 1.97	302.2 1.89
0.3		172.2 2.43	214.8 3.82	197.6 3.34	225.8 2.64		222.9 2.37	216.7 2.23	228.4 2.12
0.4	86.5 3.32	106.4 3.33	121.2 3.10	117.8 2.80	118.1 2.41		117.0 2.24	116.9 2.24	121.0 1.81
0.5	53.0 4.63	56.6 4.00	66.6 4.06	65.4 3.69	63.6 3.41		63.0 2.57	71.9 2.38	68.0 2.43
0.6	32.7 5.14	29.7 5.46	35.3 5.54	34.1 3.66	36.7 3.41		37.1 3.31	36.8 3.28	36.6 3.32
0.7	18.3 6.82	19.6 6.43	21.9 5.03	19.30 4.78	20.13 4.59		22.73 4.26	20.11 4.49	21.28 4.28
0.8	11.76 7.85	11.22 7.91	11.39 4.46			11.61 3.82			13.35 3.53
0.9	6.65 9.43	5.91 7.49	6.97 5.71			6.72 4.95			7.43 4.52
1.0	3.92 8.52	3.79 8.19	4.16 6.91			4.43 6.03			4.17 6.42
1.2	1.19 10.5	1.59 9.19	1.80 7.44			1.62 6.91			1.285 7.73
1.4	0.545 10.0		0.530 8.5						0.541 8.47
1.6	0.244 15.3		0.226 13.3						0.275 12.0
1.8	0.096 21.3		0.065 24.7						0.107 18.8
$p_T \backslash x_F$	0.01	0.02	0.025	0.03	0.04	0.05	0.06	0.075	0.1
0.05	620.4 1.75	555.9 2.03		432.9 2.10	390.7 2.01	334.4 2.41	293.4 2.81	249.6 2.34	186.3 2.76
0.1	561.5 1.62	515.0 1.51		451.6 1.69	401.9 1.74	353.7 2.04	311.8 2.39	249.7 2.10	195.6 2.45
0.15	488.0 1.52	451.4 1.59		407.1 1.87	360.3 1.51	324.8 1.76	287.8 2.07	247.8 1.69	197.1 2.03
0.2	377.0 1.62	373.1 1.58		322.5 1.89	300.2 1.74	276.8 1.66	254.2 1.91	222.0 1.59	180.0 1.85
0.25	303.3 1.73	276.3 1.73		263.0 1.90	237.6 1.83	224.7 1.94	211.0 2.19	188.8 1.52	157.5 1.69
0.3	222.1 1.97	209.5 1.98		199.6 2.07	185.9 2.34	174.1 2.13	172.3 2.29	152.1 1.59	127.5 1.76
0.4	122.2 1.79	119.6 1.75		109.7 1.90		98.3 1.39		91.0 1.34	79.4 1.39
0.5	69.8 2.42	64.5 2.54		65.2 2.61		57.4 1.89		53.2 2.01	48.73 1.62
0.6	38.0 3.25	36.8 3.34		35.7 3.44		32.88 2.39		29.98 2.56	28.95 1.98
0.7	21.10 4.28	20.32 4.43		19.74 4.56		19.31 3.06		18.06 3.40	16.10 2.30
0.8			11.28 3.72			12.03 3.84		11.09 4.17	9.69 3.15
0.9			6.82 4.89			5.57 6.32		6.28 5.61	5.61 4.30
1.0			4.30 6.19			3.61 7.93		3.50 8.18	3.45 5.43
1.2			1.228 7.83			1.48 8.21		1.33 8.96	1.220 6.85
1.4						0.512 9.62			0.479 10.8
1.6						0.223 14.3			0.225 15.4
1.8						0.062 32.4			0.113 19.2
$p_T \backslash x_F$	0.125	0.15	0.2	0.25	0.3	0.4	0.5		
0.05	165.1 3.39	140.3 3.11	111.4 3.59	96.9 4.47	77.8 5.33	39.6 7.63			
0.1	160.5 3.00	147.9 2.69	103.1 3.26	83.7 3.26	63.5 5.38	36.7 5.56	20.5 8.14		
0.15	161.6 2.48	131.2 2.36	104.3 2.80						
0.2	146.8 2.28	124.3 2.16	86.0 2.58	62.4 2.76	45.1 4.36	25.4 4.61	14.54 6.79		
0.25	130.8 2.04	108.7 1.99	72.9 2.52						
0.3	104.7 2.16	90.2 2.00	67.8 2.38	46.1 2.79	30.9 4.32	17.19 4.53	9.73 6.74		
0.4	68.7 1.64	62.34 1.50	45.50 2.06	33.00 2.84	23.63 4.21	12.21 4.61	6.98 6.93		
0.5	41.95 1.95	39.51 1.68	29.98 2.28	22.82 3.11	14.82 4.76	9.29 4.73	4.22 8.48		
0.6	24.95 2.29	23.46 2.35	18.43 2.62	16.02 3.29	11.81 4.84	5.86 5.67	2.85 8.76		
0.7		13.76 2.55	10.88 3.44						
0.8		8.33 3.17	6.72 4.28	6.30 3.32	4.51 4.87	2.56 5.18	1.49 7.43		
0.9		4.55 4.07	4.28 4.97						
1.0		2.95 4.87	2.43 6.37	2.11 5.14	1.52 7.57	0.812 8.23	0.496 11.6		
1.2		0.992 6.32	0.936 6.68	0.639 8.72	0.585 11.4	0.313 12.0	0.190 17.4		
1.4			0.358 8.33		0.268 11.2	0.136 17.2	0.078 25.3		
1.6			0.187 11.4		0.093 18.0	0.036 32.0			
1.8			0.059 23.6						

Table 4: Double differential invariant cross section  $f(x_F, p_T)$  [mb/(GeV<sup>2</sup>/c<sup>3</sup>)] for  $\pi^+$  in p+C interactions at 158 GeV/c. The statistical uncertainty  $\Delta f$  is given in %

$f(x_F, p_T), \Delta f$									
$p_T \backslash x_F$	-0.1	-0.075	-0.05	-0.04	-0.03	-0.025	-0.02	-0.01	0.0
0.05							541.6 2.35	646.3 2.19	602.6 1.57
0.1					525.3 2.11		595.9 1.74	601.7 1.48	579.8 1.43
0.15				426.5 2.81	481.8 1.88		511.6 1.69	469.1 1.60	498.6 1.39
0.2			345.9 3.01	364.0 2.74	372.4 1.97		373.7 1.80	374.9 1.68	367.2 1.66
0.25			250.1 3.30	275.0 2.53	294.5 2.00		289.2 1.96	285.9 1.91	296.1 1.78
0.3		160.4 1.77	194.6 3.50	197.4 2.89	215.5 2.34		217.1 2.22	210.9 2.18	214.0 2.06
0.4	86.2 3.33	103.3 2.58	112.8 2.75	115.3 2.49	115.2 2.09		110.7 2.17	118.6 2.03	125.7 1.75
0.5	52.8 3.62	55.8 3.24	64.6 3.53	63.0 3.29	63.3 2.80		64.7 2.54	63.5 3.03	64.4 2.50
0.6	31.2 3.99	31.7 4.10	32.7 4.91	35.5 3.61	36.6 3.43		34.2 3.47	35.5 3.35	32.1 3.51
0.7	18.5 5.01	19.4 5.14	19.0 5.45	19.31 4.79	20.88 4.44		20.31 4.44	20.02 4.42	20.30 4.48
0.8	10.64 6.32	10.38 6.41	11.76 4.68			11.74 3.77			11.12 3.81
0.9	5.98 7.84	6.63 7.38	6.64 5.63			6.66 4.98			6.72 4.95
1.0	3.84 8.72	3.83 8.14	3.79 7.56			4.21 6.32			3.78 6.43
1.2	1.29 10.2	1.46 9.30	1.26 8.87			1.30 7.78			1.246 8.62
1.4	0.491 10.6		0.506 8.94						0.582 8.21
1.6	0.205 15.8		0.189 14.8						0.184 14.3
1.8	0.093 21.4		0.101 19.7						0.075 22.4
$p_T \backslash x_F$	0.01	0.02	0.025	0.03	0.04	0.05	0.06	0.075	0.1
0.05	576.1 1.71	469.0 2.17		387.0 2.13	336.6 2.15	265.9 2.63	225.5 3.11	200.6 2.60	150.2 3.06
0.1	539.5 1.58	464.9 1.54		387.9 1.79	316.2 1.93	275.2 2.30	246.7 2.58	205.1 2.28	146.6 2.76
0.15	445.0 1.50	407.0 1.64		353.7 2.00	314.0 1.64	262.3 1.96	238.0 2.17	187.4 1.95	148.8 2.18
0.2	362.0 1.56	320.5 1.69		294.7 1.98	269.1 1.85	230.8 1.87	205.8 2.11	180.8 1.80	131.7 2.14
0.25	274.0 1.75	256.7 1.86		235.6 2.03	210.3 1.85	192.3 2.15	171.8 2.41	147.1 1.78	109.4 1.99
0.3	218.1 2.01	189.2 2.07		173.0 2.26	163.8 2.53	150.6 2.32	132.1 2.64	125.0 1.75	96.1 2.03
0.4	113.0 1.93	107.0 1.85		101.8 1.97		91.7 1.45		74.2 1.50	62.1 1.59
0.5	61.0 2.58	59.1 2.66		58.6 2.76		52.5 1.99		44.9 2.20	38.85 1.81
0.6	35.2 3.37	33.4 3.53		28.5 3.91		28.46 2.61		26.50 2.65	23.85 2.22
0.7	18.92 4.53	18.74 4.68		17.40 4.91		17.13 3.32		15.10 3.77	13.10 2.66
0.8			10.58 3.96			9.07 4.35		8.98 4.65	7.62 3.43
0.9			6.44 5.14			5.64 6.23		5.06 6.06	4.36 5.00
1.0			3.28 6.71			3.84 7.43		2.83 9.23	2.63 6.22
1.2			1.376 7.42			1.03 9.86		1.06 10.1	1.007 7.38
1.4						0.440 10.6			0.449 11.0
1.6						0.150 18.3			0.197 16.3
1.8						0.050 36.2			0.064 28.7
$p_T \backslash x_F$	0.125	0.15	0.2	0.25	0.3	0.4	0.5		
0.05	111.9 3.92	86.1 3.94	55.1 5.14	41.4 6.81	33.3 8.22	12.1 13.6			
0.1	117.8 3.44	81.8 3.66	58.1 4.55	41.8 4.75	29.4 7.69	10.8 10.2	5.1 16.2		
0.15	111.0 2.92	83.1 2.86	51.4 3.80						
0.2	98.8 2.64	81.9 2.54	53.5 3.27	30.7 3.96	22.7 6.11	9.6 7.61	4.34 12.4		
0.25	90.7 2.42	72.7 2.41	42.6 3.28						
0.3	73.4 2.57	58.2 2.49	39.3 3.09	25.9 3.72	17.2 5.71	7.69 6.83	3.23 11.8		
0.4	50.5 1.92	42.19 1.79	28.69 2.55	18.31 3.77	12.21 5.83	5.33 7.03	2.10 13.0		
0.5	31.78 2.23	27.36 2.03	21.15 2.72	14.13 3.93	9.79 5.88	3.83 7.61	1.57 13.3		
0.6	19.02 2.67	17.09 2.71	12.00 3.30	9.28 4.51	6.12 6.83	3.07 7.43	0.97 15.1		
0.7		10.30 2.99	7.40 4.17						
0.8		5.97 3.68	5.12 4.74	3.75 4.29	2.60 6.45	1.20 7.56	0.56 12.0		
0.9		3.60 4.57	2.65 6.31						
1.0		2.28 5.58	1.73 7.50	1.45 6.22	0.95 9.62	0.588 9.57	0.189 15.2		
1.2		0.727 7.42	0.674 7.96	0.540 9.49	0.392 13.7	0.173 16.9	0.077 27.1		
1.4			0.293 9.42		0.150 14.3	0.063 25.7	0.031 39.6		
1.6			0.106 14.0		0.064 21.6	0.026 32.3			
1.8			0.037 24.4						

Table 5: Double differential invariant cross section  $f(x_F, p_T)$  [mb/(GeV<sup>2</sup>/c<sup>3</sup>)] for  $\pi^-$  in p+C interactions at 158 GeV/c. The statistical uncertainty  $\Delta f$  is given in %

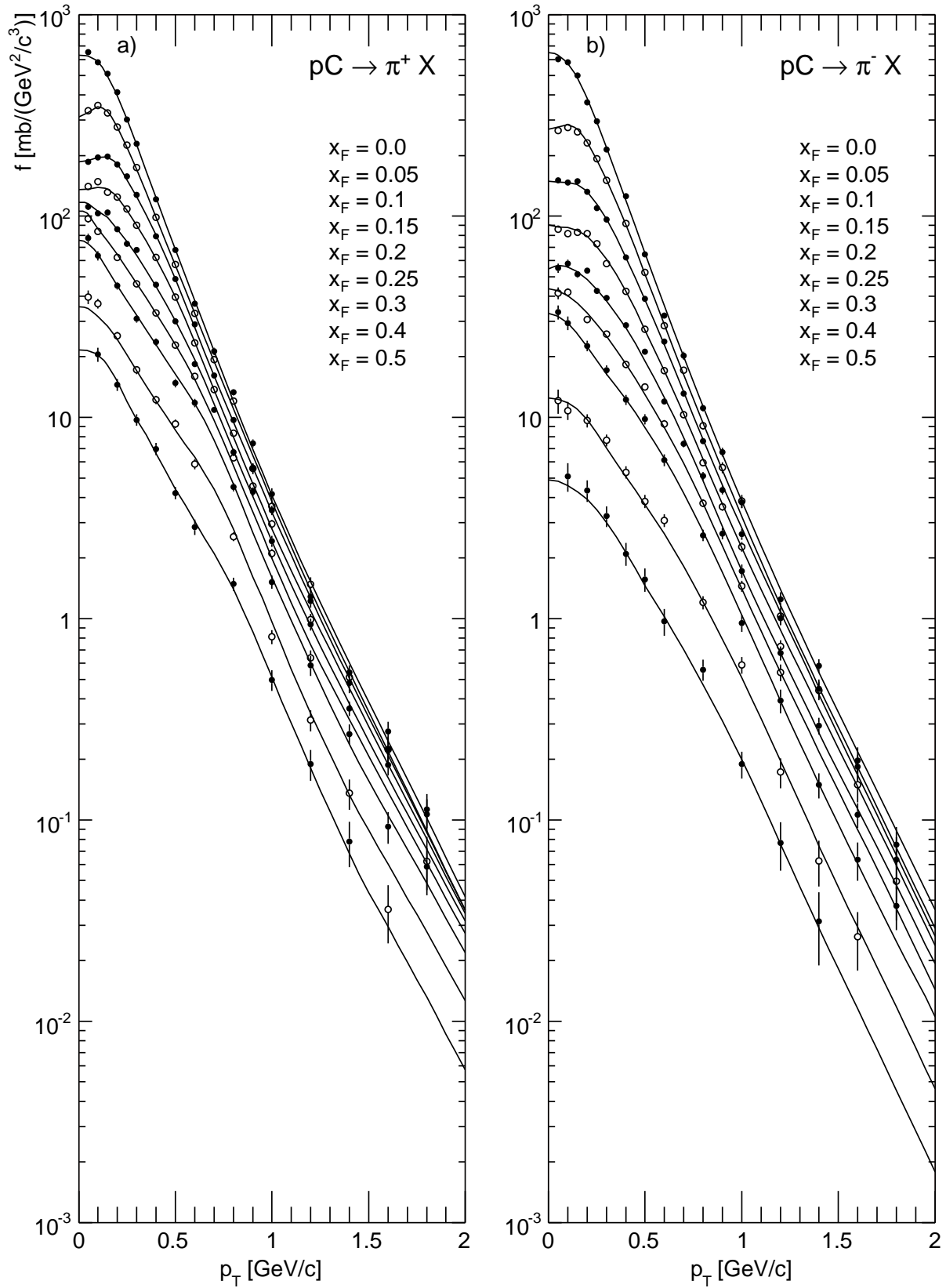


Figure 17: Invariant cross section as a function of  $p_T$  at fixed  $x_F$  for a)  $\pi^+$  and b)  $\pi^-$  produced in p+C collisions at 158 GeV/c

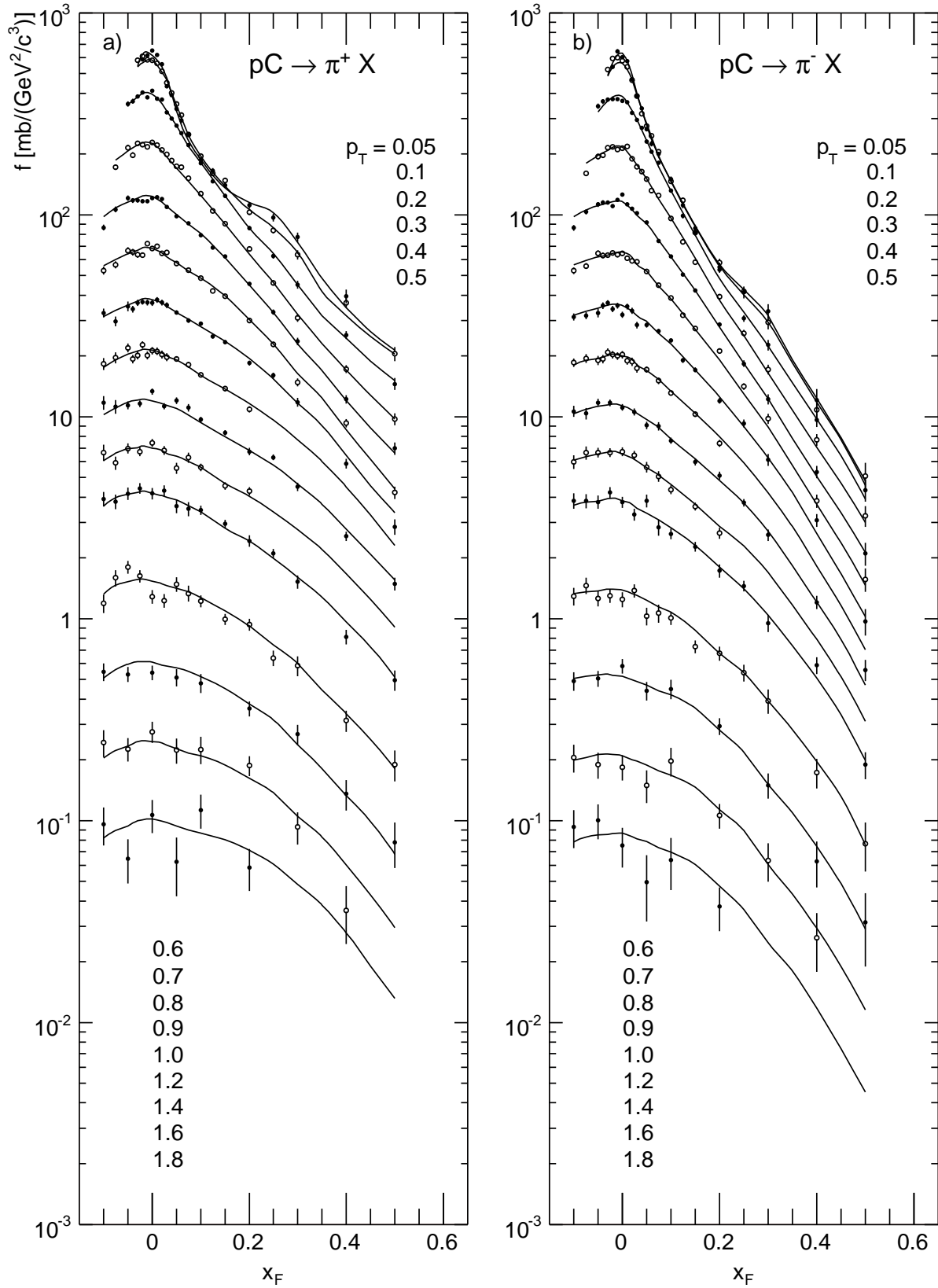


Figure 18: Invariant cross section as a function of  $x_F$  at fixed  $p_T$  for a)  $\pi^+$  and b)  $\pi^-$  produced in p+C collisions at 158 GeV/c

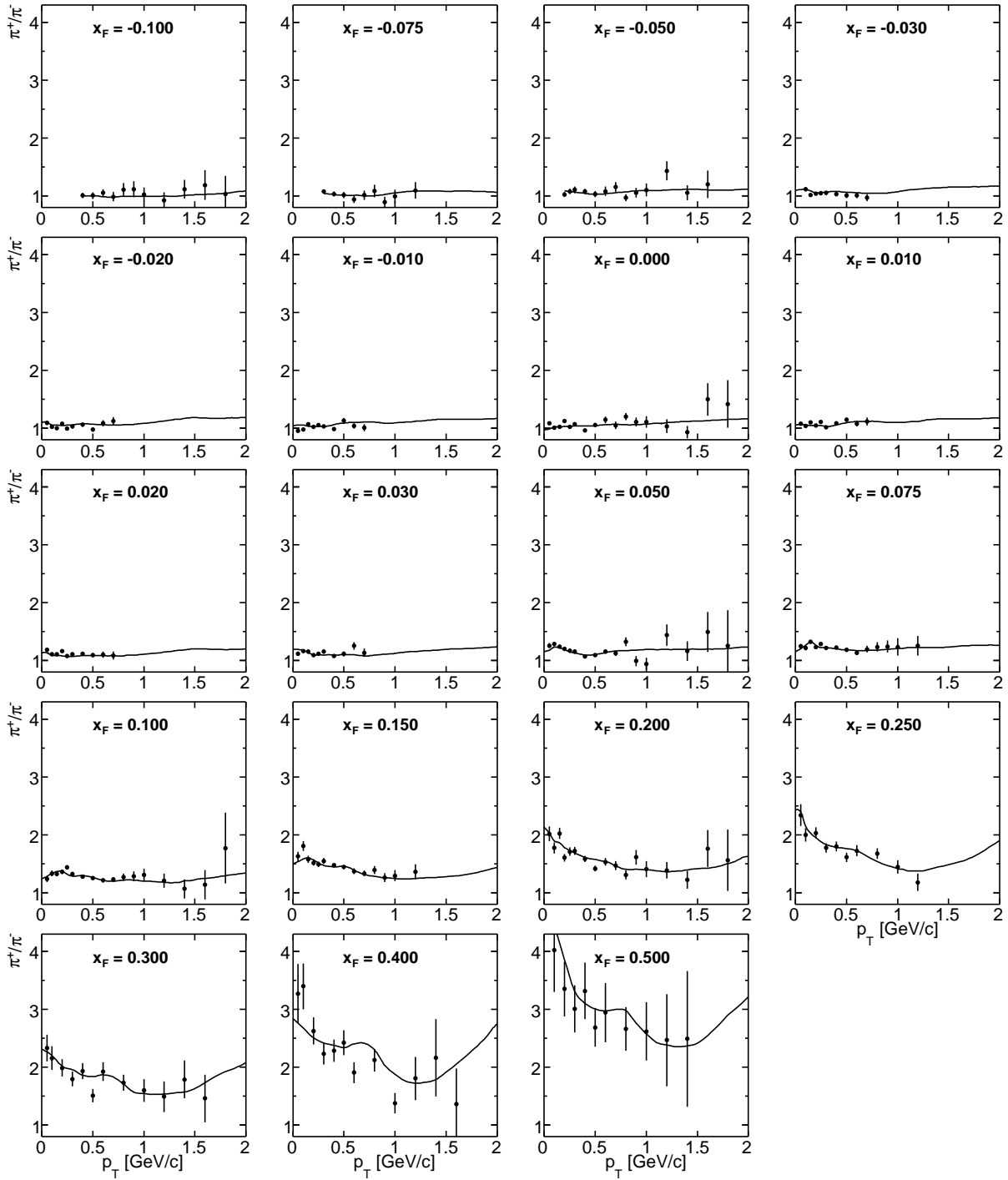


Figure 19: Ratio of invariant cross section for  $\pi^+$  and  $\pi^-$  as a function of  $p_T$  at fixed  $x_F$ . The lines represent the result of the data interpolation

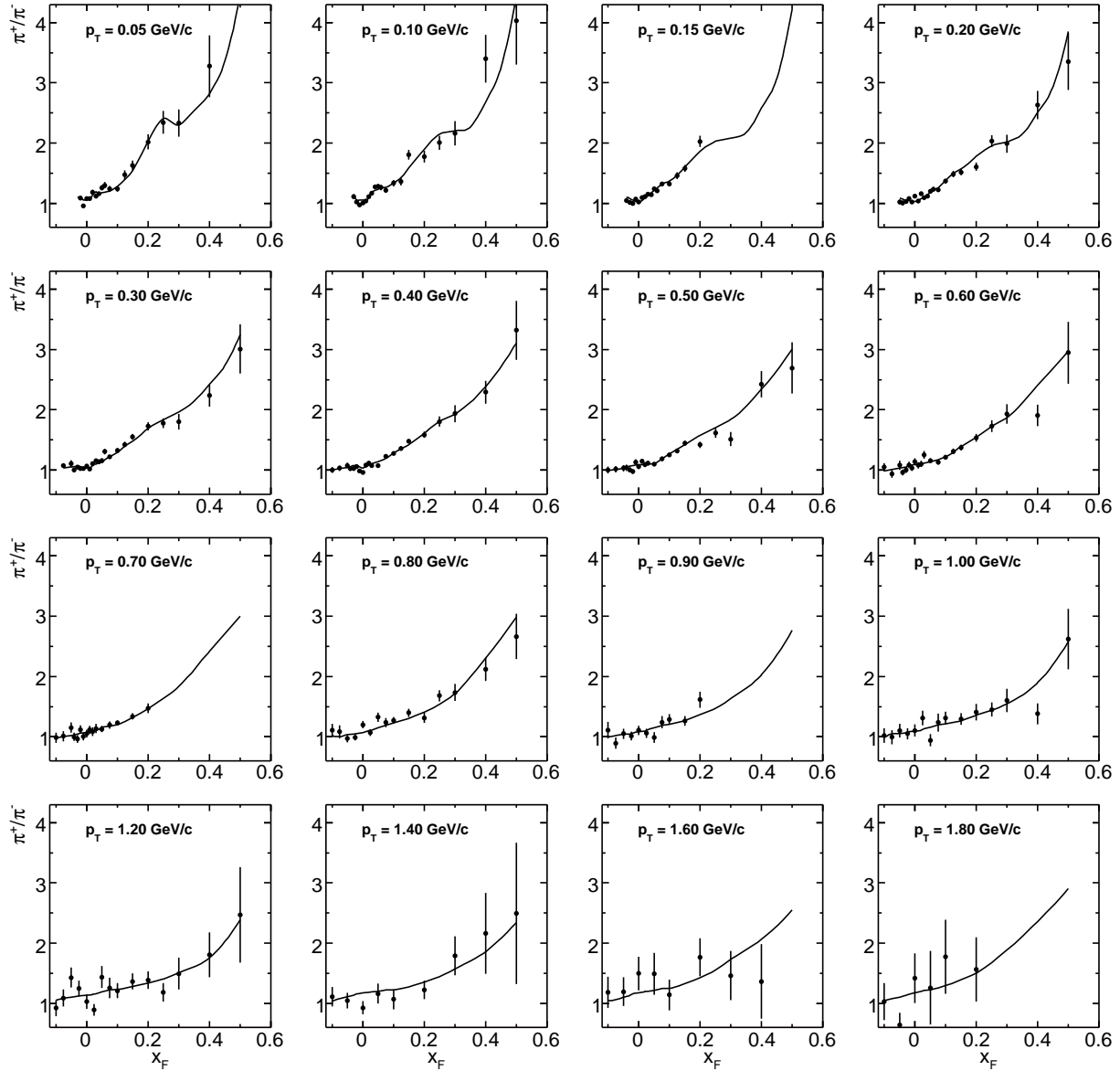


Figure 20: Ratio of invariant cross section for  $\pi^+$  and  $\pi^-$  as a function of  $x_F$  at fixed  $p_T$

This comparison shows global similarities. Remarkable differences are however visible in the backward direction where the ratios are expected to approach unity due to the isoscalar nature of the target nucleus, and in the detailed structures in the projectile hemisphere.

### 5.3 Rapidity and transverse mass distributions

The rapidity distributions at fixed  $p_T$  presented in Fig. 21 extend up to 1.5 units into the target hemisphere at  $p_T < 0.4$  GeV/c and therefore allow a clear view of the asymmetry which reaches about 0.25 units at low  $p_T$ .

In comparison to p+p collisions [1], they show an important steepening in the projectile hemisphere at all transverse momenta, whereas the characteristic deformation at low  $p_T$  and  $y$  is still clearly visible. The  $m_T$  distributions for both charges are shown in Fig. 22.

As stressed in [1] these distributions are all but exponential and the variation of the local inverse slopes  $T$  with  $m_T$ , shown in Fig. 23, is even more pronounced than in p+p collisions.

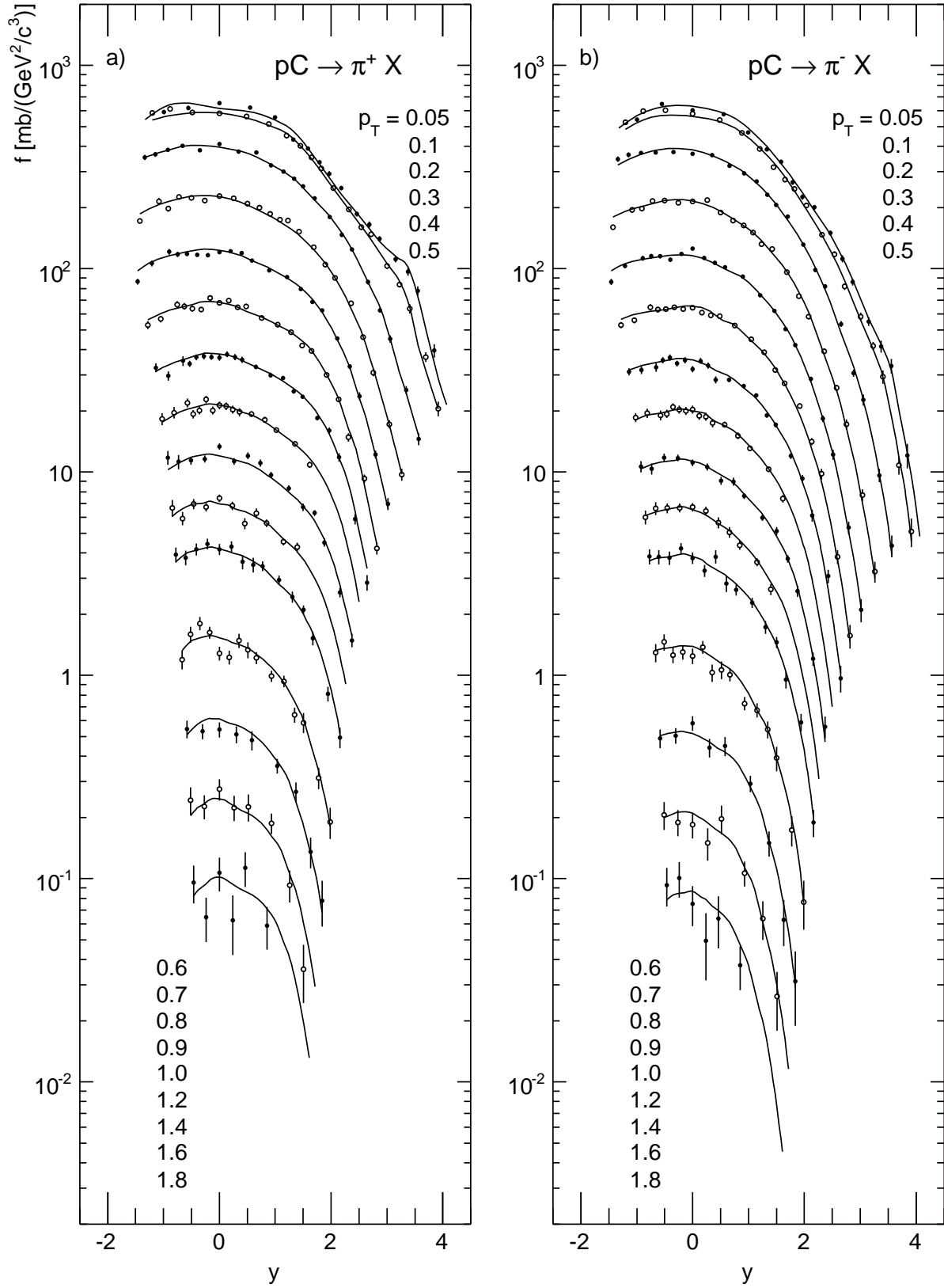


Figure 21: Invariant cross section as a function of  $y$  at fixed  $p_T$  for a)  $\pi^+$  and b)  $\pi^-$  produced in p+C collisions at 158 GeV/c

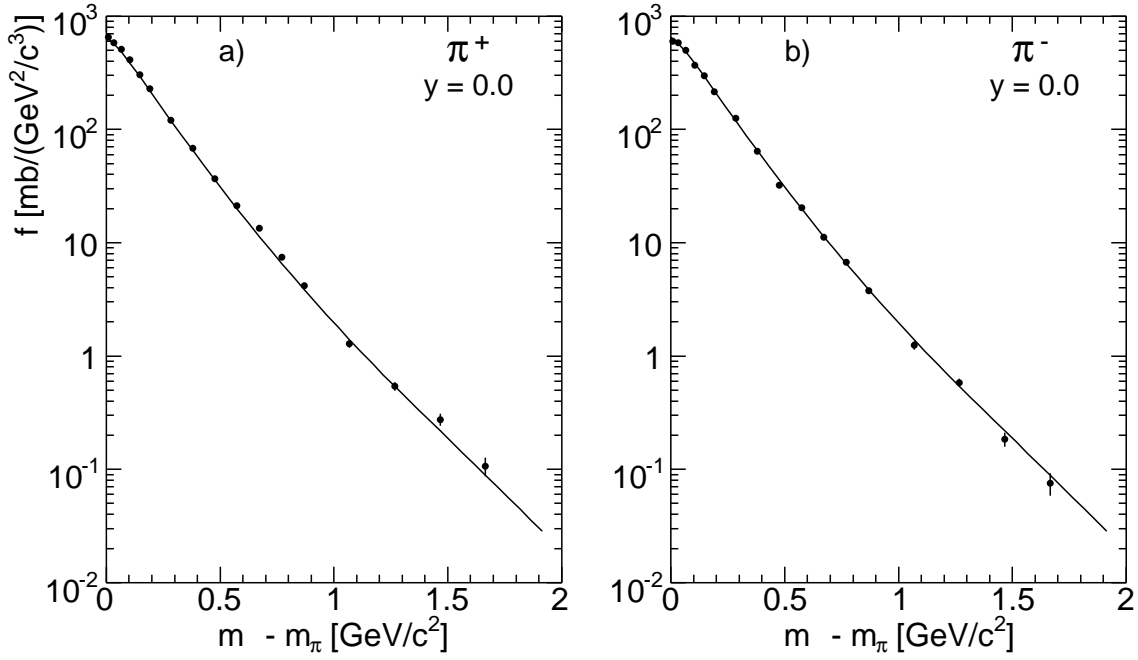


Figure 22: Invariant cross section as a function of  $m_T - m_\pi$  for a)  $\pi^+$  and b)  $\pi^-$  produced at  $y = 0.0$

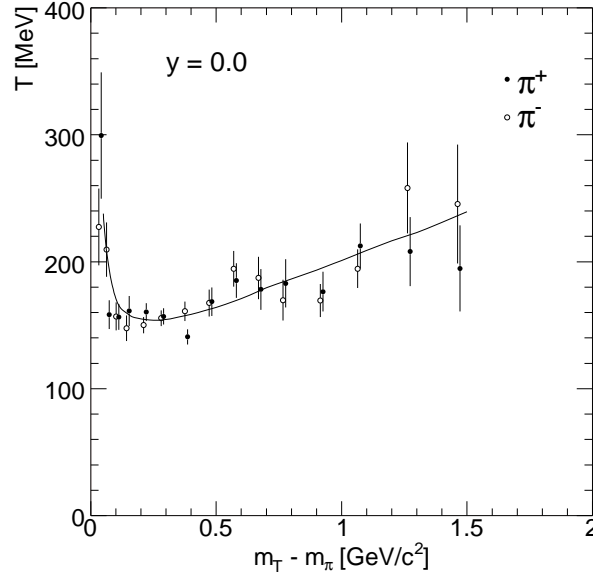


Figure 23: Local slope of the  $m_T$  distribution as a function of  $m_T - m_\pi$  for  $\pi^+$  and  $\pi^-$ . The line shown is to guide the eye

## 6 Comparison to other data

As shown in Sect. 2, the only existing data set which can be directly compared to the NA49 results is that of Barton et al.[7]. This comparison is shown in Fig. 24.

For the 10 points which overlap with the NA49 data a clear upward deviation with an average of +25% or 3.6 standard deviations is evident. This deviation is somewhat hard to understand as these results come from a group which has published results on p+p interactions with the same apparatus [14] which show excellent agreement with NA49 (see [1] for a detailed



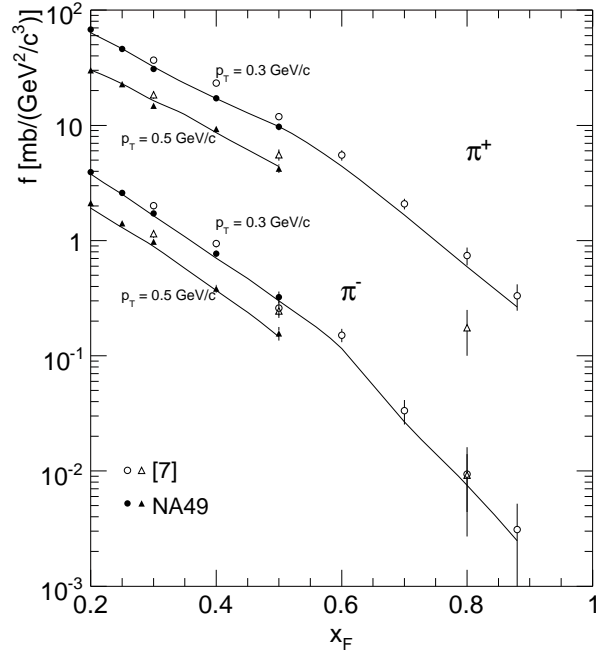


Figure 24: Comparison of the invariant cross section as a function of  $x_F$  at fixed  $p_T$  from NA49 (full symbols) with measurement from [7] (open symbols). The  $\pi^-$  data lines are multiplied by 0.1 to allow a separation from the  $\pi^+$

discussion). Also the p+p reference data obtained in the framework of [7] are internally consistent, notwithstanding their sizable statistical errors, both with [14] and with NA49. Preliminary analysis reveals the same problem also with proton yields in p+C collisions.

As the differences are similar for both pion charges, the  $\pi^+/\pi^-$  ratios are expected to be unaffected by the problem. This is indeed the case, the good agreement between the two data sets at  $p_T = 0.3$  GeV/c as a function of  $x_F$  is shown in Fig. 25.

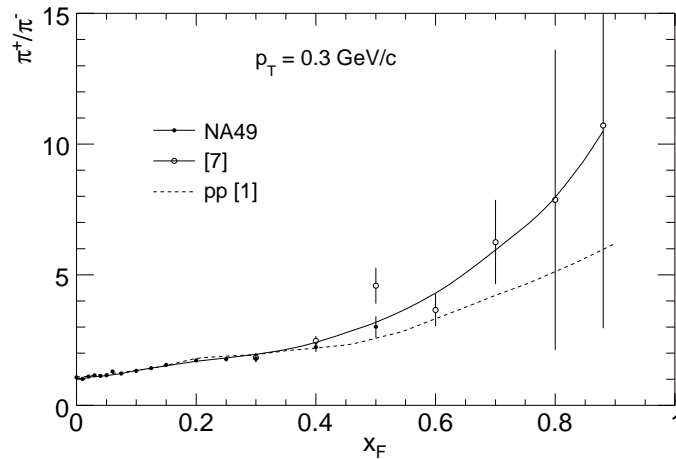


Figure 25: Comparison of the  $\pi^+/\pi^-$  ratio as a function of  $x_F$  at fixed  $p_T$  from NA49 (full circles) with measurement from [7] (open circles). The dashed line represents the p+p data [1]

Since the Barton [7] data extend up to  $x_F = 0.88$  at their measured transverse momenta, one can use the consistency of the  $\pi^+/\pi^-$  ratio to extend the NA49 data - albeit with large error bars - into the region of large  $x_F$ . This shows, as indicated in Fig. 25, a sizable increase

of the charge ratio with respect to the p+p data also given in the Fig. It is also possible, under the assumption that the large systematic yield difference has no dependence on  $p_T$  or  $x_F$ , to extend the interpolation of the NA49 data towards large  $x_F$  by imposing a 25% reduction on the Barton et al. data. This extension is also indicated in Fig. 24 for  $p_T = 0.3$  GeV/c. It shows the characteristic break in the  $x_F$  dependence at  $x_F$  between 0.5 and 0.6 also visible in the p+p data [1].

## 7 Integrated distributions

The  $p_T$  integrated yields

$$\begin{aligned}
 dn/dx_F &= \pi/\sigma_{\text{inel}} \cdot \sqrt{s}/2 \cdot \int f/E \cdot dp_T^2 \\
 F &= \int f \cdot dp_T^2 \\
 dn/dy &= \pi/\sigma_{\text{inel}} \cdot \int f \cdot dp_T^2
 \end{aligned} \tag{5}$$

are obtained from the interpolated data. The numerical values are given in Table 6 and presented as functions of  $x_F$  and  $y$  in Fig. 26.

$x_F$	$\pi^+$						$\pi^-$						$y$	$\pi^+$ $dn/dy$	$\pi^-$ $dn/dy$				
	$F$	$\Delta$	$dn/dx_F$	$\Delta$	$\langle p_T \rangle$	$\Delta$	$\langle p_T^2 \rangle$	$\Delta$	$F$	$\Delta$	$dn/dx_F$	$\Delta$				$\langle p_T \rangle$	$\Delta$	$\langle p_T^2 \rangle$	$\Delta$
-0.05	64.312	0.57	13.211	0.57	0.3267	0.40	0.1533	0.80	60.470	0.57	12.401	0.57	0.3287	0.40	0.1543	0.80	-0.6	0.9795	0.9311
-0.04	66.736	0.52	15.726	0.52	0.3114	0.31	0.1411	0.60	62.771	0.52	14.749	0.52	0.3141	0.31	0.1425	0.60	-0.4	0.9994	0.9521
-0.03	69.546	0.48	19.030	0.48	0.2954	0.30	0.1287	0.55	65.076	0.48	17.768	0.48	0.2970	0.31	0.1294	0.55	-0.2	1.0120	0.9688
-0.02	72.264	0.38	23.052	0.38	0.2801	0.28	0.1177	0.52	68.061	0.38	21.743	0.38	0.2796	0.30	0.1168	0.55	0.0	1.0010	0.9646
-0.01	73.693	0.34	26.993	0.34	0.2658	0.27	0.1077	0.50	69.751	0.33	25.747	0.33	0.2631	0.30	0.1049	0.54	0.2	0.9796	0.9317
0.0	71.923	0.32	28.088	0.32	0.2586	0.27	0.1030	0.48	69.484	0.30	27.364	0.30	0.2558	0.30	0.1008	0.54	0.4	0.9373	0.8751
0.01	70.586	0.32	25.756	0.32	0.2672	0.27	0.1088	0.50	66.470	0.31	24.424	0.31	0.2648	0.30	0.1062	0.55	0.6	0.8941	0.8159
0.02	66.086	0.32	20.903	0.32	0.2840	0.27	0.1210	0.50	60.877	0.32	19.247	0.32	0.2844	0.30	0.1206	0.55	0.8	0.8448	0.7597
0.03	61.594	0.33	16.683	0.33	0.3012	0.29	0.1339	0.55	55.378	0.35	14.938	0.35	0.3042	0.31	0.1352	0.58	1.0	0.7898	0.6905
0.04	57.541	0.35	13.389	0.35	0.3205	0.30	0.1491	0.60	50.685	0.37	11.757	0.37	0.3237	0.32	0.1506	0.62	1.2	0.7291	0.6131
0.05	54.137	0.35	10.981	0.35	0.3379	0.32	0.1637	0.62	47.027	0.38	9.516	0.38	0.3413	0.32	0.1649	0.62	1.4	0.6611	0.5296
0.075	46.426	0.35	7.067	0.35	0.3734	0.32	0.1957	0.62	38.142	0.38	5.790	0.38	0.3781	0.32	0.1993	0.62	1.6	0.5807	0.4451
0.1	40.396	0.35	4.904	0.35	0.3960	0.30	0.2182	0.58	31.456	0.38	3.803	0.38	0.4045	0.32	0.2268	0.62	1.8	0.4942	0.3612
0.125	35.101	0.37	3.531	0.37	0.4144	0.32	0.2375	0.65	25.590	0.42	2.561	0.42	0.4277	0.33	0.2525	0.65	2.0	0.4069	0.2806
0.15	30.875	0.38	2.648	0.38	0.4267	0.32	0.2520	0.65	21.385	0.47	1.826	0.47	0.4436	0.34	0.2708	0.70			
0.2	23.488	0.50	1.5499	0.50	0.4489	0.37	0.2797	0.70	14.535	0.62	0.9555	0.62	0.4730	0.37	0.3053	0.70			
0.25	18.174	0.65	0.9734	0.65	0.4607	0.41	0.2967	0.80	10.258	0.87	0.5475	0.87	0.4909	0.43	0.3308	0.85			
0.3	13.327	0.87	0.5996	0.87	0.4755	0.44	0.3154	0.90	7.105	1.15	0.3190	1.15	0.4993	0.53	0.3425	1.10			
0.4	7.207	1.15	0.2455	1.15	0.4912	0.61	0.3344	1.10	3.060	1.60	0.1041	1.60	0.5159	0.63	0.3664	1.15			
0.5	3.943	1.60	0.1081	1.60	0.4714	0.90	0.3157	1.60	1.226	2.40	0.0336	2.40	0.5125	1.00	0.3620	2.00			

Table 6:  $p_T$  integrated invariant cross section  $F$  [mb·c], density distribution  $dn/dx_F$ , mean transverse momentum  $\langle p_T \rangle$  [GeV/c], mean transverse momentum squared  $\langle p_T^2 \rangle$  [(GeV/c)<sup>2</sup>] as a function of  $x_F$ , as well as density distribution  $dn/dy$  as a function of  $y$  for  $\pi^+$  and  $\pi^-$ . The statistical uncertainty  $\Delta$  for each quantity is given in %

The  $p_T$  integrated  $\pi^+/\pi^-$  ratios, and the first and second moments of the  $p_T$  distributions are shown as functions of  $x_F$  in Fig. 27.

Due to the absence of data with sufficient phase space coverage allowing for integration over transverse momentum, a comparison with other experiments is unfortunately not possible.

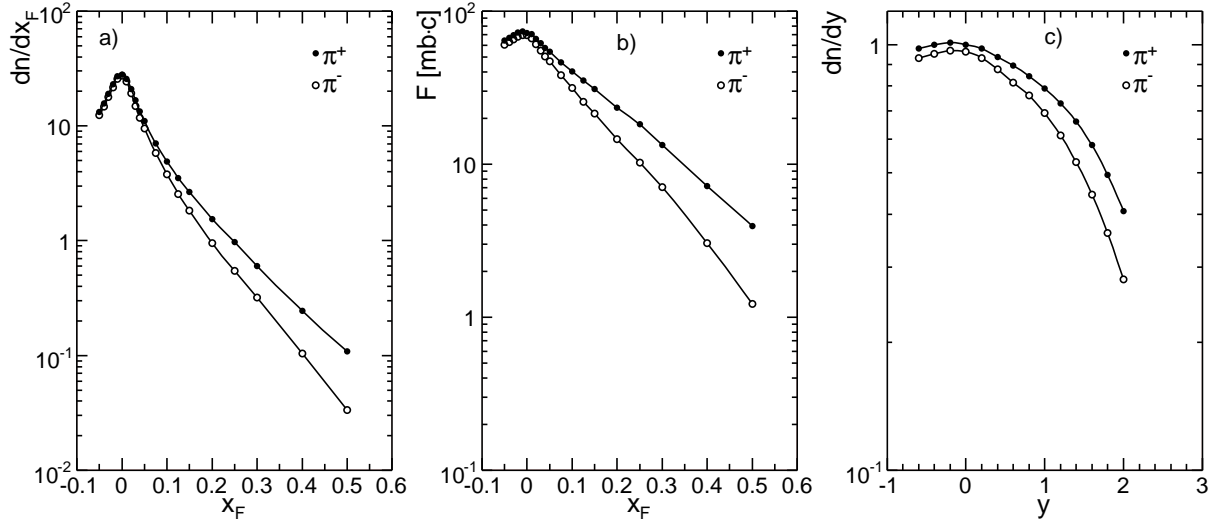


Figure 26: Integrated distributions of  $\pi^+$  and  $\pi^-$  produced in p+C interactions at 158 GeV/c: a) density distribution  $dn/dx_F$  as a function of  $x_F$ ; b) invariant cross section  $F$  as a function of  $x_F$ ; c) density distribution  $dn/dy$  as a function of  $y$

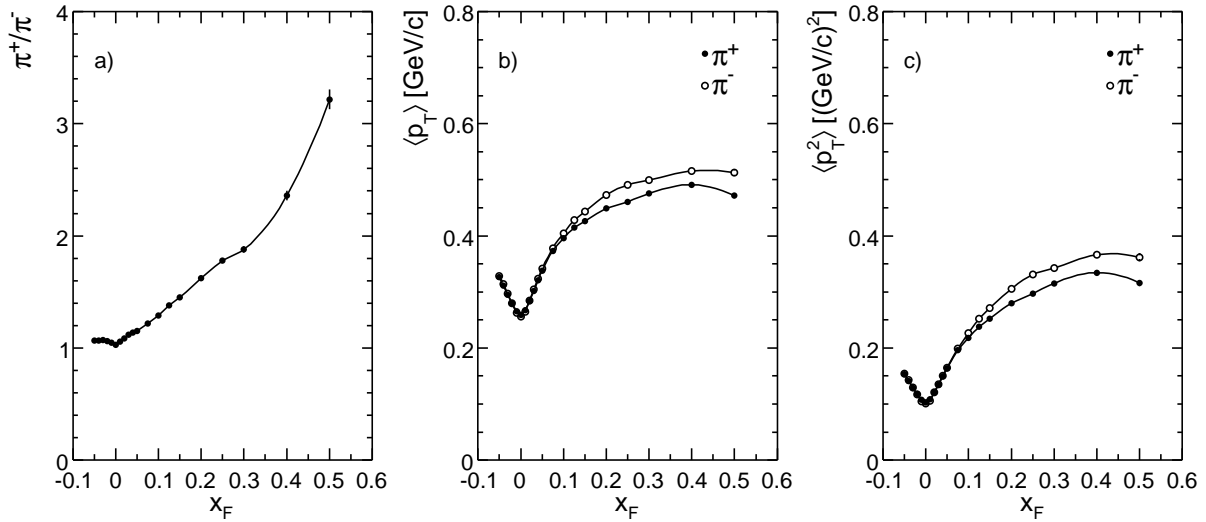


Figure 27: a)  $\pi^+/\pi^-$  ratio, b) mean  $p_T$ , and c) mean  $p_T^2$  as a function of  $x_F$  for  $\pi^+$  and  $\pi^-$  produced in p+C interactions at 158 GeV/c

## 8 Dependence on the number of grey protons

Due to the large fraction of single projectile collisions in minimum bias p+C interactions, the number of grey protons  $n_{\text{grey}}$  measured in this reaction has a steep maximum at zero counts, as shown in Fig. 3 above. Correspondingly the event sample decreases rapidly from 377 000 to 102 000 and 26 000 respectively by selecting events with one or two grey protons. A general study of double differential inclusive cross sections as described above is therefore not feasible for these subsamples with reasonable statistical errors. On the other hand grey proton selection allows an important extension of the physics analysis since it effectively suppresses the contribution of peripheral collisions in favour of more central events with multiple projectile collisions.

The problem of limited statistics can be overcome by extracting the  $p_T$  integrated yields

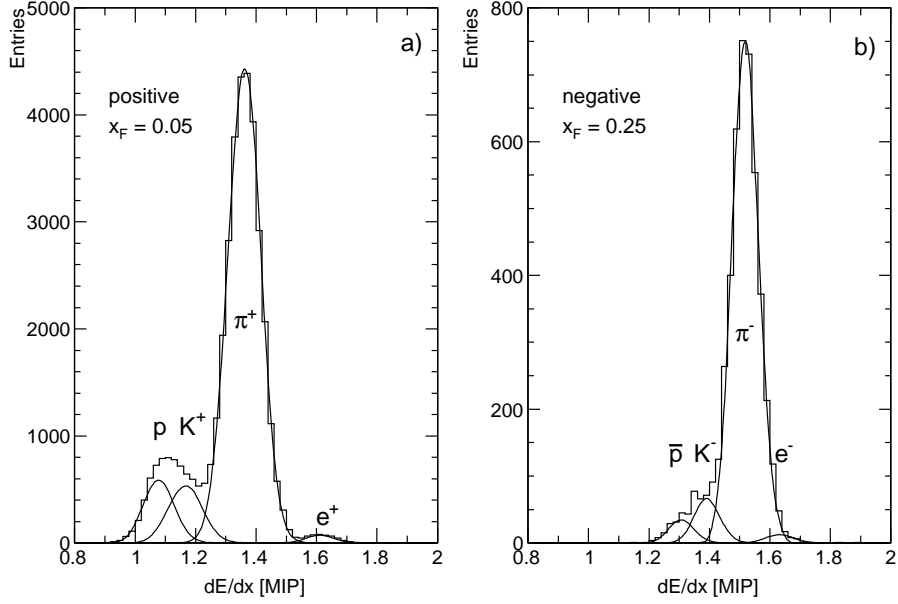


Figure 28:  $dE/dx$  for  $p_T$  integrated fits for a)  $\pi^+$  and b)  $\pi^-$

directly from the data sample as a function of  $x_F$  only. There is a limit to this procedure set by the necessities of particle identification. The variation of the total momentum over the chosen bin width in  $x_F$  must be small enough to allow for the necessary resolution of the energy loss distribution. At low  $x_F$  this variation becomes prohibitive due to the strong variation of the total momentum with  $p_T$ . The method is therefore limited to  $x_F \geq 0.025$ . The quality of the  $dE/dx$  distributions obtained is shown in Fig. 28 for two values of  $x_F$ .

The extracted  $p_T$  integrated pion yields are given in Table 7 for the total minimum bias sample and for the two centrality selections  $n_{\text{grey}} \geq 1$  and  $n_{\text{grey}} \geq 2$ . The distributions have been corrected by using the treatment developed in Sect. 4 integrated over transverse momentum. The yields obtained for the minimum bias event sample are in good statistical agreement with the values obtained from the integration of the interpolated double differential cross sections given in Table 6.

In comparison to the  $x_F$  dependence in minimum bias condition, a systematic steepening is observed as shown in Figs. 29a and 30a for  $\pi^+$  and  $\pi^-$ , respectively. The difference

	$\pi^+$						$\pi^-$					
	minimum bias		$n_{\text{grey}} \geq 1$		$n_{\text{grey}} \geq 2$		minimum bias		$n_{\text{grey}} \geq 1$		$n_{\text{grey}} \geq 2$	
$x_F$	$dn/dx_F$	$\Delta$	$dn/dx_F$	$\Delta$	$dn/dx_F$	$\Delta$	$dn/dx_F$	$\Delta$	$dn/dx_F$	$\Delta$	$dn/dx_F$	$\Delta$
0.025	18.920	0.7	21.198	1.2	22.872	2.3	17.175	0.7	18.968	1.3	21.157	2.5
0.05	10.996	0.6	11.875	1.0	12.704	2.0	9.469	0.5	10.509	0.9	11.179	1.6
0.10	4.908	0.6	5.045	1.1	5.270	2.2	3.793	0.8	3.935	1.4	4.036	2.8
0.15	2.641	0.7	2.649	1.3	2.806	2.6	1.810	1.0	1.848	1.9	1.961	3.6
0.20	1.536	1.0	1.463	1.8	1.510	3.6	0.977	1.2	0.966	2.2	0.960	4.4
0.25	0.969	1.2	0.877	2.4	0.880	4.7	0.540	1.6	0.556	3.0	0.547	6.0
0.30	0.592	1.5	0.549	3.0	0.526	6.1	0.322	2.4	0.308	4.0	0.292	8.2
0.35	0.399	1.8	0.337	3.8	0.3032	8.1	0.174	3.0	0.153	5.7	0.1872	10.2
0.40	0.243	2.3	0.216	4.8	0.1793	10.5	0.107	3.5	0.0989	7.1	0.0933	14.5
0.50	0.0973	3.6	0.0785	8.0	0.0672	17.2	0.0337	6.2	0.0298	12.9		

Table 7:  $dn/dx_F$  for  $n_{\text{grey}}$  selection. The uncertainty  $\Delta$  is given in %

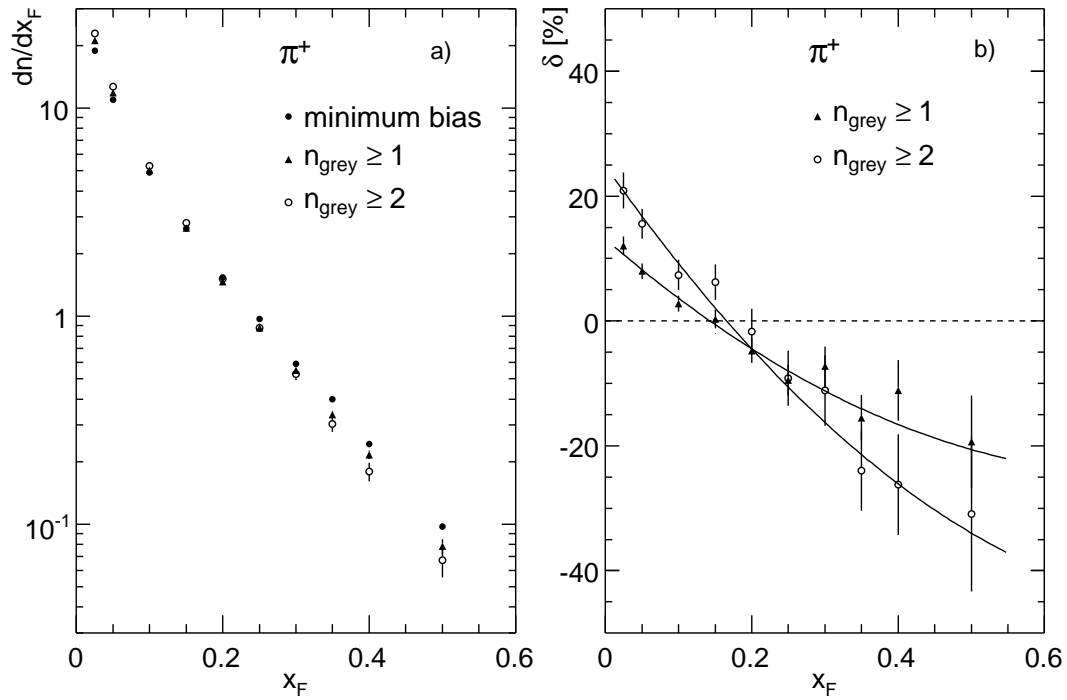


Figure 29: a)  $dn/dx_F$  for  $n_{\text{grey}}$  selection and b) the difference  $\delta$  between samples with  $n_{\text{grey}}$  selection and minimum bias for  $\pi^+$ . The lines shown are to guide the eye

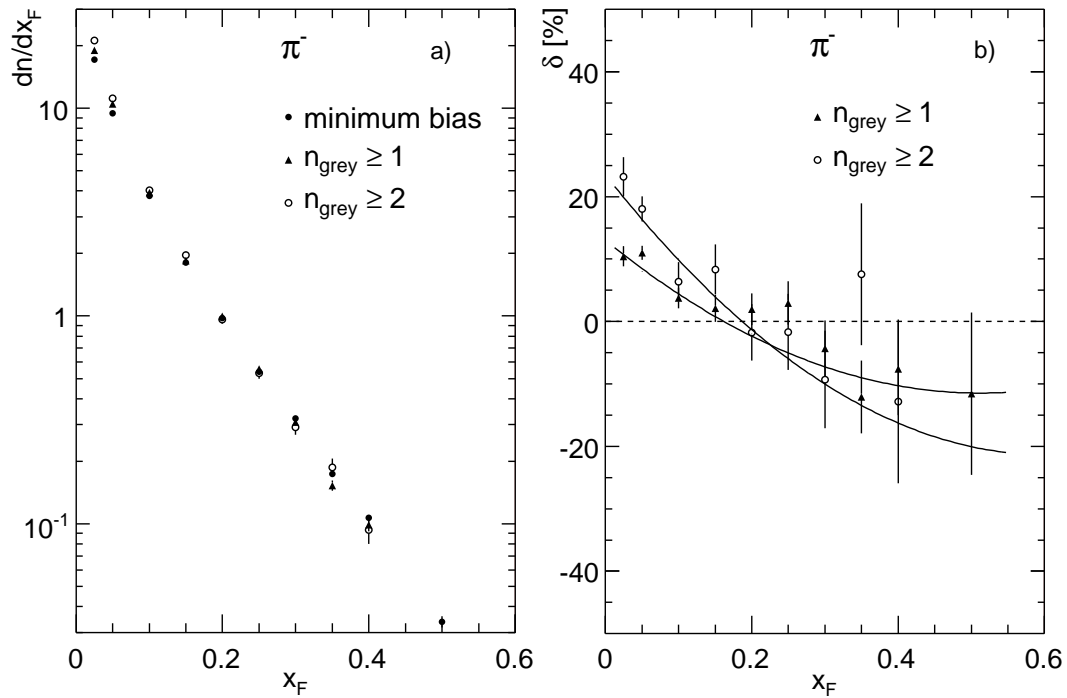


Figure 30: a)  $dn/dx_F$  for  $n_{\text{grey}}$  selection and b) the difference  $\delta$  between samples with  $n_{\text{grey}}$  selection and minimum bias for  $\pi^-$ . The lines shown are to guide the eye

$\delta(dn/dx_F) = ((dn/dx_F)_{n_{\text{grey}}} - (dn/dx_F)_{\text{min. bias}}) / (dn/dx_F)_{n_{\text{grey}}}$  is shown separately in Figs. 29b and 30b.

## 9 Availability of the presented data

As in [1] the tabulated values of NA49 data are available in numerical form on the Web Site [16]. In addition two sets of  $\pi^+$  and  $\pi^-$  momentum vectors ( $5 \times 10^7$  each) can be found on this site. They are generated via Monte Carlo following the data interpolation presented in Sect. 5 between the limits  $-0.1 < x_F < 0.5$  and  $0 < p_T < 2$  GeV/c using a slight extrapolation of the data in the backward hemisphere at low  $p_T$  and to  $p_T$  values beyond 1.8 GeV/c. Normalized invariant distributions may be deduced from these vectors using the inelastic cross section given in Sect. 3.2 and the following total integrated pion multiplicities in the  $x_F$  range from -0.1 to +0.5:

$$\begin{aligned}\langle n_{\pi^+} \rangle &= 3.279 \\ \langle n_{\pi^-} \rangle &= 2.909\end{aligned}$$

## 10 Conclusions

A new set of inclusive cross sections on pion production in minimum bias p+C collisions at the CERN SPS is presented. The data cover the central production region within the total range of  $-0.1 < x_F < 0.5$  and  $0 < p_T < 1.8$  GeV/c for the first time. The statistical uncertainties are typically at the few percent level over the 270 measured bins per charge, with systematic errors of less than 5%. A detailed discussion of the results, including in particular an in-depth comparison to the recently published data from NA49 on p+p interactions, will be presented in an accompanying paper.

## Acknowledgements

This work was supported by the Bundesministerium für Bildung und Forschung, Germany, the Polish State Committee for Scientific Research (1 P03B 006 30, SPB/CERN/P-03/Dz 446/2002-2004, 2 P03B 04123), the Hungarian Scientific Research Foundation (T032648, T032293, T043514), the Hungarian National Science Foundation, OTKA, (F034707), the Polish-German Foundation, the Bulgarian National Science Fund (Ph-09/05), the EU FP6 HRM Marie Curie Intra-European Fellowship Program, and the Particle Physics and Astronomy Research Council (PPARC) of the United Kingdom.

## References

- [1] C. Alt et al., Eur. Phys. J. **C45** (2006) 343
- [2] H. G. Fischer et al., Nucl. Phys. **A715** (2003) 118
- [3] MINOS Technical Design Report NuMI-L-337 (1998)
- [4] T. K. Gaisser and M. Honda, Ann. Rev. Nucl. Part. Sci. **52**, 153 (2002)
- [5] M. Bonesini et al., Eur. Phys. J. **C20** (2001) 13  
N. V. Mokhov et al., AIP Conf. Proc. **435** (1997) 543  
A. J. Malensek, Fermilab-FN341 (1981)
- [6] Proposal CERN-SPSC/P322 (2001)
- [7] D. Barton et al., Phys. Rev. **D27** (1983) 2580
- [8] N. A. Nikiforov et al., Phys. Rev. **C22** (1980) 700
- [9] S. Afanasiev et al., Nucl. Instrum. Meth. **A430** (1999) 210
- [10] M. K. Hegab and J. Hüfner, Nucl. Phys. **A384** (1982) 353
- [11] K. Braune et al., Z. Phys. **C13** (1982) 191
- [12] M. K. Hegab and J. Hüfner, Phys. Lett. **B105** (1981) 103
- [13] G. Bellettini et al., Nucl. Phys. **79** (1966) 609  
A. Carroll et al., Phys. Lett. **B80** (1979) 319  
B. Bobchenko et al., Sov. J. Nucl. Phys. **30** (1979) 805  
S. Denisov et al., Nucl. Phys. **B61** (1973) 62  
A. Ashmore et al., Phys. Rev. Lett. **5** (1960) 576
- [14] A. E. Brenner et al., Phys. Rev. **D26** (1982) 1497
- [15] D. Drijard et al., Nucl. Instrum. Meth. **225** (1984) 367
- [16] <http://cern.ch/spshadrons>
- [17] Baryon and charged kaon production in p+C interaction, NA49 collaboration (to be published)